

**SELECTED PROBLEMS IN TURBULENCE THEORY AND
MODELING**

A Dissertation

by

EUN-HWAN JEONG

Submitted to the Office of Graduate Studies of
Texas A&M University
in partial fulfillment of the requirements for the degree of

DOCTOR OF PHILOSOPHY

December 2003

Major Subject: Aerospace Engineering

**SELECTED PROBLEMS IN TURBULENCE THEORY AND
MODELING**

A Dissertation

by

EUN-HWAN JEONG

Submitted to Texas A&M University
in partial fulfillment of the requirements
for the degree of

DOCTOR OF PHILOSOPHY

Approved as to style and content by:

Sharath S. Girimaji
(Chair of Committee)

Ali Beskok
(Member)

Othon Rediniotis
(Member)

Walter E. Haisler
(Head of Department)

Paul Cizmas
(Member)

December 2003

Major Subject: Aerospace Engineering

ABSTRACT

Selected Problems in Turbulence Theory and Modeling.

(December 2003)

Eun-Hwan Jeong, B.S.; M.S. Korea Advanced Institute of
Science and Technology, Korea

Chair of Advisory Committee: Dr. Sharath S. Girimaji

Three different topics of turbulence research that cover modeling, theory and model computation categories are selected and studied in depth. In the first topic, “velocity gradient dynamics in turbulence” (modeling), the Lagrangian linear diffusion model that accounts for the viscous-effect is proposed to make the existing restricted-Euler velocity gradient dynamics model quantitatively useful. Results show good agreement with DNS data. In the second topic, “pressure-strain correlation in homogeneous anisotropic turbulence subject to rapid strain-dominated distortion” (theory), extensive rapid distortion calculation is performed for various anisotropic initial turbulence conditions in strain-dominated mean flows. The behavior of the rapid pressure-strain correlation is investigated and constraining criteria for the rapid pressure-strain correlation models are developed. In the last topic, “unsteady computation of turbulent flow past a square cylinder using partially-averaged Navier-Stokes method” (model computation), the basic philosophy of the PANS method is reviewed and a practical problem of flow past a square cylinder is computed for various levels of physical resolution. It is revealed that the PANS method can capture many important unsteady flow features at an affordable computational effort.

DEDICATION

To my wife, Jeong-Min, and my daughters, Seo-Hyun and Juwon.

ACKNOWLEDGMENTS

I would like to express my deepest appreciation to my committee chairman, Dr. Sharath S. Girimaji, for his support, guidance, patience and providing me with opportunities to learn from his talent and wide/deep experience.

I am also grateful to Dr. Othon Rediniotis, Dr. Paul Cizmas, and Dr. Ali Beskok for their help as committee members. I am also thankful to Dr. N. K. Anand for his advice and help.

I wish to express my thanks to my Korean colleagues in the aerospace engineering department and my neighbors for the memorable times that we shared together.

This accomplishment might not have been possible without the care, encouragement, patience, and support of my family in Korea: parents, parents-in-law, sister, sister-in-law, brothers, and brothers-in-law.

Finally, I would like to give special thanks to my wife, Jeong-Min Ahn, and my daughters, Seo-Hyun and Juwon, for their love, sacrifice, and encouragement.

TABLE OF CONTENTS

	Page
ABSTRACT	iii
DEDICATION.....	iv
ACKNOWLEDGMENTS.....	v
TABLE OF CONTENTS.....	vi
LIST OF TABLES	viii
LIST OF FIGURES.....	ix
 CHAPTER	
I INTRODUCTION.....	1
1.1 Velocity gradient dynamics in turbulence.....	2
1.2 Pressure-strain correlation in homogeneous anisotropic turbulence subject to rapid strain-dominated distortion.....	3
1.3 Unsteady computation of turbulent flow past a square cylinder using partially-averaged Navier-Stokes method	3
 II VELOCITY GRADIENT DYNAMICS IN TURBULENCE : EFFECT OF VISCOSITY AND FORCING.....	5
2.1 Introduction	5
2.2 Velocity gradient evolution equation	7
2.3 Lagrangian analysis and modeling	10
2.4 Result and discussion	16
2.5 Conclusion.....	20
 III PRESSURE-STRAIN CORRELATION IN HOMOGENEOUS ANISOTROPIC TURBULENCE SUBJECT TO RAPID STRAIN- DOMINATED DISTORTION.....	29
3.1 Introduction	29
3.2 Governing equations.....	34
3.3 Calculation procedure.....	37
3.4 Results and discussion.....	40
3.5 Conclusion.....	50

CHAPTER	Page
IV UNSTEADY COMPUTATION OF TURBULENT FLOW PAST A SQUARE CYLINDER USING PARTIALLY-AVERAGED NAVIER-STOKES (PANS) METHOD.....	63
4.1 Introduction	63
4.2 PANS model equations	65
4.3 Computation	70
4.4 Results and discussion.....	71
4.5 Conclusion.....	75
REFERENCES.....	87
APPENDIX A	91
VITA	93

LIST OF TABLES

TABLE	Page
3.1 Model coefficients for expression (3.12)	52
3.2 Summary of RDT and IP, LRR, SSG model calculation results	53
3.3 IP, LRR, SSG model behavior assessment in RD limit	54
4.1 The computational geometry and resolution control parameter setting ...	77
4.2 Summary of the PANS calculation result of integrated flow parameters in comparison with experiment and LES data	77

LIST OF FIGURES

FIGURE	Page
2.1 Typical R - Q trajectory of the restricted-Euler model. Dotted line represents $D = 27R^2/4 + Q^3 = 0$	22
2.2 Typical R - Q trajectory of the LDM	23
2.3 Typical R - Q trajectory of the LLDM	24
2.4 R - Q scatter plot of DNS result for isotropic turbulence with small wavenumber forcing ($Re_{\lambda}=90$, Yeung ¹⁴).....	25
2.5 R - Q scatter plot of forced LLDM at nearly steady state	26
2.6 Normalized probability density functions of viscous diffusion terms in forced LLDM. Variable= $\nu \nabla^2 Y / \sigma(\nu \nabla^2 Y) = (-C_{pq} C_{pq} Y / 3 \tau_L) / \sigma(-C_{pq} C_{pq} Y / 3 \tau_L)$. σ =standard deviation. $Y = a_{ij}, s_{ij}$ or ω_{ij}	27
2.7 Plot of conditional average of viscous diffusion versus corresponding variables in forced LLDM. Conditional mean= $\langle \nu \nabla^2 Y Y \rangle / \sigma(\nu \nabla^2 Y)$, equation (2.36). $Y = a_{ij}, s_{ij}$ or ω_{ij}	28
3.1 Coordinate scheme for the 2C3 initial turbulence state	55
3.2 Evolution of the ratio $R1$ for various cases, a) HS (1C2), b) AE (2C2), c) AC (2C2), d) PS (2C2).....	56
3.3 Evolution of $P''_{ij} b_{ij}$ and $\Phi^{(r)}_{ij} b_{ij}$, a) PS (isotropic), b) HS (1C2), c) AE (2C2), d) AC (2C2), e) PS (2C2)	57
3.4 AC flow with 1C2 initial turbulence state: a) Lumley triangle, b) evolution of the $R1$ parameter, c) evolution of $P''_{ij} b_{ij}$ and $\Phi^{(r)}_{ij} b_{ij}$	58
3.5 HS flow with 1C1 initial turbulence state: a) Lumley triangle, b) evolution of the $R1$ parameter, c) evolution of $P''_{ij} b_{ij}$ and $\Phi^{(r)}_{ij} b_{ij}$	59
3.6 PS flow with 1C1 initial turbulence state: a) Lumley triangle, b) evolution of the $R1$ parameter, c) evolution of $P''_{ij} b_{ij}$ and $\Phi^{(r)}_{ij} b_{ij}$	60

FIGURE	Page
3.7 AE flow with 1C2 initial turbulence state: a) Lumley triangle, b) evolution of the $R1$ parameter, c) evolution of $P''_{ij}b_{ij}$ and $\Phi^{(r)}_{ij}b_{ij}$	61
3.8 Solution trajectories in the Lumley triangle, a) AC (2C2 and isotropic), b) PS (2C2 and isotropic).....	62
4.1 Computational domain	78
4.2 Time step/grid size convergence test result of flow past a cylinder in 2D domain, (a) time step convergence test result, (b) grid size convergence test result	79
4.3 Instantaneous contour plot of velocity magnitude (a-c), z-vorticity (d-f), unresolved kinetic energy (g-i), and unresolved eddy viscosity (j-l) for various f_k value	80
4.4 Stream-wise mean velocity profiles along the centerline	81
4.5 Profiles of $((u'u')_{\text{mean}})^{1/2}$, $((v'v')_{\text{mean}})^{1/2}$, and $((w'w')_{\text{mean}})^{1/2}$ along the centerline	82
4.6 Instantaneous iso-surfaces, (a)-(b) vorticity magnitude, (c)-(d) velocity magnitude, (e)-(f) z-velocity, (g)-(h) x-vorticity, and (i)-(j) y-vorticity..	83
4.7 Lateral profiles of mean velocities at various x-locations	85
4.8 Lateral profiles of turbulent quantities at various x-locations	86

CHAPTER I

INTRODUCTION

Turbulence is one of the most complicated types of fluid motion. In this irregular, highly diffusive, and dissipative fluid motion, wide range spectrum of the scale of motion exists. Starting from the largest eddies, energy is cascaded into smaller and smaller eddies through non-linear interactions and is finally dissipated by viscous action at the smallest eddies. It is very difficult to generalize this broad ranged fluctuating motion. These complicated flow features are solely governed by the Navier-Stokes equation. However, the general solution for this non-linear equation is not known, and the solutions are strongly influenced by the boundary/initial conditions. Furthermore, solving Navier-Stokes equation exactly (namely, direct numerical simulation: DNS) for a specific turbulent flow requires overwhelming computing power because of the broad range of scales of motions. Currently, DNS is only possible for relatively simple, low-Reynolds number flows and is used more as numerical experiments of canonical flows. Consequently, for practical applications, we need turbulence models. To construct adequately accurate turbulence models, a clear understanding of the underlying physics is important.

The turbulence research area can be roughly categorized as physical/numerical experiment, theory, and modeling. The experiment is the most fundamental method in turbulence research. Through direct measurement / computation of the flow of interest,

This dissertation follows the style and format of Physics of Fluids.

quantitative or qualitative information on turbulent flow is acquired. Analytical or mathematical way of describing turbulent physics is sought in turbulence theory category. Ultimately, theory and experiment results are directly used in the development of turbulence models.

In this dissertation, three different topics that cover *modeling*, *theory* and, additionally, *model computation* categories are chosen. They are i) velocity gradient dynamics in turbulence (modeling); ii) pressure-strain correlation in homogeneous anisotropic turbulence subject to rapid strain-dominated distortion (theory); and iii) unsteady computation of turbulent flow past a square cylinder using partially-averaged Navier-Stokes method (model computation). Each topic is discussed independently in depth in the separate chapters. The purpose and research directions are as follows.

1.1 VELOCITY GRADIENT DYNAMICS IN TURBULENCE

Knowledge of the velocity gradient dynamics is essential for understanding of wide ranged turbulence motions: turbulent kinetic energy cascade to the smaller scale is closely related to the vortex stretching mechanism and the velocity gradient performs a crucial role in this vortex-stretching phenomenon; scalar mixing and evolution of material surfaces are also related to the velocity gradient tensor; the dissipation of the turbulent kinetic energy is statistics of velocity gradient. Currently, there exists a simple velocity gradient dynamic model called the restricted-Euler equation. The restricted-Euler equation explains many of qualitative features of turbulent flow observed in experiments. However, in the restricted-Euler equation, viscous and anisotropic pressure Hessian effects are absent. Inadequate viscous-effect modeling causes velocity-gradients to diverge in finite time. In this research, we develop new model that accounts for the viscous-effect-variable relaxation time scale model-to resolve the unphysical behavior

of restricted-Euler model. The results are compared with DNS data.

1.2 PRESSURE-STRAIN CORRELATION IN HOMOGENEOUS ANISOTROPIC TURBULENCE SUBJECT TO RAPID STRAIN-DOMINATED DISTORTION

In the Reynolds stress closure, the modeling of pressure-strain correlation term is one of the toughest tasks. Pressure is usually decomposed into slow and rapid pressure. The role of the pressure-strain correlation is different depends on the turbulent flow regime. In return to isotropy turbulence regime, production is absent. Only the dissipation and the slow pressure-strain correlation affect the turbulence evolution. On the contrary, the slow pressure and dissipation terms are absent in rapid distortion limit. In this limit, the mean flow deformation rate is much larger than turbulent strain rate. As a result, turbulent flow is governed by a set of linear equations (rapid distortion theory: RDT). In this research, rapid distortion calculation is performed for various anisotropic initial turbulence conditions in strain-dominated mean flows. The behavior of the rapid pressure-strain correlation is investigated and constraining criteria for the rapid pressure-strain correlation models are sought.

1.3 UNSTEADY COMPUTATION OF TURBULENT FLOW PAST A SQUARE CYLINDER USING PARTIALLY-AVERAGED NAVIER-STOKES METHOD

For accurate prediction of unsteady turbulent flow, it is necessary to resolve large unsteady scales of motion to some extent. Large Eddy Simulation (LES) and Direct Numerical Simulation (DNS) are physically appropriate tools for this purpose but computationally unaffordable for practical engineering applications. As a bridging model between RANS and LES, partially-averaged Navier-Stokes (PANS) method has

been proposed recently. In this research, basic philosophy of PANS method is reviewed and, as a practical application, flow past a square cylinder is computed for various levels of physical resolution. The results are compared extensively with existing experimental and LES data.

CHAPTER II

VELOCITY GRADIENT DYNAMICS IN TURBULENCE: EFFECT OF VISCOSITY AND FORCING

In this chapter, the first topic, “velocity gradient dynamics in turbulence” is discussed. The restricted-Euler equation is a promising but incomplete model for velocity-gradient dynamics in turbulent flows. While it captures many of the geometric features of the vorticity vector and the strain rate tensor, viscous and anisotropic–pressure Hessian effects are not accounted for satisfactorily. Inadequate viscous-effect modeling causes velocity-gradients to diverge in finite time, rendering the restricted-Euler model unsuitable for practical applications. We perform a Lagrangian frame analysis to fully comprehend the physics of viscous relaxation time-scale and propose a variable time-scale model that can adequately account for deformation history. Most importantly, the finite-time singularity (divergence of velocity-gradients) problem is fully resolved with the present model. We also model the effects of forcing that is used in numerical simulations to sustain stationary isotropic turbulence. Detailed comparison of the new model with DNS data reveals good agreement.

2.1 INTRODUCTION

Velocity-gradient dynamics and small-scale structure offer unique insight into turbulence mechanisms such as energy cascade, intermittency, material-element deformation, scalar mixing, etc. Important turbulence process such as vortex stretching and gradient-steepening due to non-linear interactions appear explicitly in the fluctuating

velocity-gradient equations making them well-suited for studying turbulence physics. Recently, details of many aspects of velocity-gradient dynamics and small-scale structures have emerged from direct numerical simulations (DNS). Some of the observed behavior lack simple explanations and while others are completely contrary to previous expectations. The objective of this chapter (and similar studies in the past of Ashurst et. al¹, Girimaji and Pope², Cantwell^{3,4}, Girimaji and Speziale⁵, Soria et. al⁶, Martin et. al^{7,8,9}, Ooi et. al¹⁰) is to develop simple dynamical models to explain the observed small-scale behavior.

The restricted-Euler equation, first proposed by Viellefosse¹¹, captures many of the qualitative aspects of the small-scale structure^{1,3}. Cantwell⁴ performed detailed studies of the velocity-gradient invariants to demonstrate further agreement between the restricted-Euler dynamical model and DNS data. The original restricted-Euler model had three major deficiencies : (i) incompatibility with mean momentum equation; (ii) lack of anisotropic pressure Hessian effects; and (iii) lack of viscous effects. The first of these deficiencies has been decisively addressed by Girimaji and Speziale⁶. Despite some progress, our inability to accurately account for anisotropic-pressure Hessian and viscous effects continue to limit the usefulness of the restricted-Euler model. Of the two, viscous effects are particularly important since the inviscid assumption leads to finite-time singularity (divergence) of the restricted-Euler equation. Currently, the only model available to account for the viscous-effects is the linear diffusion model (LDM)^{7,8}, which is based on the interaction-by-exchange with mean (IEM) and the least-mean-square estimator (LMSE) principles used for scalar mixing. The linear diffusion model assumes that the time-scale of viscous relaxation is uniform everywhere, ignoring the effects of intermittency. The LDM equations can still lead to finite-time singularity if the initial velocity gradients are large enough. In a real turbulent flow, the viscous relaxation

time-scale is distributed over a wide range of values⁷ depending on the deformation history of the fluid element. High values of velocity gradients are typically associated with faster (smaller) relaxation time scales so that the gradients always remain bounded. We address the finite-time singularity and viscosity related issues in this research. Anisotropic pressure-Hessian modeling is not considered. As pointed out by Viellefosse¹¹, this term only has a redistributive effect on the magnitude of velocity-gradients. Thus, while the omission of this may affect some qualitative aspects of velocity-gradient geometry, the finite-time singularity aspect is unaffected.

The primary objectives of present work are (i) to develop a better understanding of the viscous effects by performing Lagrangian-frame analysis and (ii) to derive a suitable variable relaxation time-scale model. A prerequisite for the model is that velocity gradients remain finite, consistent with Navier-Stokes physics. Most importantly, the effort in this research should contribute towards making the restricted-Euler based velocity-gradient model a viable computational tool. A secondary objective is to account for the effects of forcing on velocity-gradients. Small wavenumber forcing is typically employed in DNS to maintain a statistically stationary isotropic turbulent velocity field. The effect of forcing is absent in the restricted-Euler model and must be included to perform a clean comparison with forced isotropic DNS data. In anisotropic flows, turbulence production is the forcing term and that appears in closed form in the modified restricted Euler equation (Girimaji and Speziale⁵). Since the forcing is absent in practical flows, it is not considered in great detail.

2.2 VELOCITY GRADIENT EVOLUTION EQUATION

For incompressible flow, the evolution equation for the local instantaneous velocity gradient tensor, $a_{ij} = \partial u_i / \partial X_j$, is given by

$$\frac{\partial a_{ij}}{\partial t} + u_k \frac{\partial a_{ij}}{\partial X_k} + a_{ik} a_{kj} = -\frac{\partial^2 p}{\partial X_i \partial X_j} + \nu \frac{\partial^2 a_{ij}}{\partial X_k \partial X_k} \quad (2.1)$$

and the Poisson equation for kinetic pressure is

$$\frac{\partial^2 p}{\partial X_i \partial X_i} = -a_{mn} a_{nm}. \quad (2.2)$$

The strain rate tensor and vorticity vector associated with a_{ij} are given by

$$s_{ij} = \frac{1}{2}(a_{ij} + a_{ji}); \quad \omega_i = \varepsilon_{ijk} a_{kj} \quad (2.3)$$

where ε_{ijk} is the permutation index. The eigenvalues of s_{ij} are taken to be a_1, a_2 and a_3

in descending order of numerical value. Due to continuity, we have

$$a_1 + a_2 + a_3 = 0. \quad (2.4)$$

Thus, we can conclude that $a_1 > 0$ and $a_3 < 0$. The sign of a_2 is not known *a priori*.

Using (2.2), equation (2.1) can be written as

$$\frac{da_{ij}}{dt} + a_{ik} a_{kj} - \frac{1}{3} a_{mn} a_{nm} \delta_{ij} = h_{ij} \quad \text{where} \quad \frac{d}{dt} = \frac{\partial}{\partial t} + u_k \frac{\partial}{\partial X_k}. \quad (2.5)$$

In above equation, h_{ij} is composed of anisotropic pressure Hessian and viscous diffusion

terms :

$$h_{ij} \equiv -\left(\frac{\partial^2 p}{\partial X_i \partial X_j} - \frac{1}{3} \frac{\partial^2 p}{\partial X_k \partial X_k} \delta_{ij} \right) + \nu \frac{\partial^2 a_{ij}}{\partial X_k \partial X_k}. \quad (2.6)$$

The dynamics of the velocity gradient tensor can be understood by studying the behavior of its invariants P, Q and R (Cantwell²):

$$P = -a_{ii} = 0 \text{ (continuity)}; \quad Q = -a_{ij} a_{ji} / 2; \quad R = -a_{ij} a_{jk} a_{ki} / 3. \quad (2.7)$$

The characteristic equation of velocity gradient tensor is given by $\lambda^3 + Q\lambda + R = 0$ where

λ is the eigenvalue of a_{ij} . The discriminant of this characteristic equation is given by

$$D = 27R^2 / 4 + Q^3. \quad (2.8)$$

As shown by Chong et. al¹², the two-dimensional state space (R, Q) can be divided into four regions of distinct local flow topologies according to the sign of discriminant D and invariant R . The evolution equations for Q and R are :

$$\frac{dQ}{dt} = -3R - a_{ik}h_{ki}; \quad \frac{dR}{dt} = \frac{2}{3}Q^2 - a_{ij}a_{jk}h_{ki}. \quad (2.9)$$

If we assume that pressure Hessian term is isotropic and neglect viscous effects, we get the original restricted-Euler equation :

$$\frac{dQ}{dt} = -3R; \quad \frac{dR}{dt} = \frac{2}{3}Q^2; \quad \frac{dD}{dt} = 0. \quad (2.10)$$

In this autonomous system of equations, the invariants evolve along the constant discriminant line and diverge in finite time. In a turbulent flow field, viscous effects prevent the velocity gradients from getting too large. Martin et. al⁸ attempt to account for viscous effect using the linear diffusion model (LDM):

$$v \frac{\partial^2 a_{ij}}{\partial X_k \partial X_k} = -\frac{a_{ij}}{\tau_E} \quad (2.11)$$

where τ_E is a constant, interpreted as the viscous relaxation time-scale. With this model, the equations for the invariants become :

$$\frac{dQ}{dt} = -3R - 2\frac{Q}{\tau_E}; \quad \frac{dR}{dt} = \frac{2}{3}Q^2 - 3\frac{R}{\tau_E}; \quad \frac{dD}{dt} = -6\frac{D}{\tau_E}. \quad (2.12)$$

This is also an autonomous dynamical system of equations that can be solved knowing the initial conditions. This system has one attracting fixed point at the origin ($Q=0, R=0$) in the phase plane. The basin of attraction is approximately $|a_{ij}(0)a_{ij}(0)| \leq 1/\tau_E^2$. If the initial values are larger, the velocity gradient still diverges in finite time. Thus, LDM is also not completely adequate as it can, and does, permit finite-time singularity. In a turbulent flow field, the effective viscous relaxation time-scale at any point depends

on the prevailing length-scale (ℓ) at that location :

$$\tau_{eff} \sim \frac{\ell^2}{\nu}. \quad (2.13)$$

The length-scale (ℓ) depends on the deformation history of the fluid element. It can vary from the integral length-scale of turbulence to the Kolmogorov-length scale. Physically, LDM does not account for the dependence of relaxation time-scale on fluid element deformation history. It is well known that viscous dissipation (equivalently, viscous action) is intermittent in character. The spatial distribution of viscous dissipation is sporadic rather than uniform, with much of the dissipation occurring in a small fraction of the total flow field. The implication clearly is that the viscous relaxation time-scale is not constant throughout a turbulent flow field. A physically accurate model for the viscous effect must account for this variation in the time-scale due to deformation history.

2.3 LAGRANGIAN ANALYSIS AND MODELING

2.3.1 Lagrangian linear diffusion model

The dependence of viscous action on velocity gradient time history can be best understood by performing a Lagrangian frame analysis. We will consider the flow equations in a Lagrangian frame of reference (\mathbf{x}, t). The underlying Eulerian flow field is given by $\mathbf{u}(\mathbf{X}, t)$, where \mathbf{X} represents Eulerian (Cartesian) coordinate system. The Eulerian coordinate \mathbf{X} of a Lagrangian particle identified by \mathbf{x} evolves according to

$$\frac{d\mathbf{X}(\mathbf{x}, t)}{dt} = \mathbf{u}(\mathbf{X}(\mathbf{x}, t), t) \text{ with } \mathbf{X}(0) = \mathbf{x}. \quad (2.14)$$

The technique used here to study material element deformation is fairly common place in the field of continuum mechanics. In continuum mechanics terminology, the Eulerian

coordinate system can be considered as the present configuration and the Lagrangian one as the reference configuration. In the absence of material deformation caused by velocity field, the present (Eulerian) and the reference (Lagrangian) frames would be the same. The effect of the velocity field is to deform the configuration rendering the present coordinate different from the reference coordinate frame. The transformation tensor between the two frames contains important information about the material deformation.

In the Lagrangian reference frame, the evolution equation for fluctuating velocity becomes

$$\frac{du_i(\mathbf{x},t)}{dt} = -\frac{\partial p}{\partial X_i} + \nu \frac{\partial^2 u_i}{\partial X_k \partial X_k}. \quad (2.15)$$

From the equation (2.1), the Lagrangian frame evolution equation for a_{ij} can be written as

$$\frac{d}{dt} a_{ij}(\mathbf{x},t) + a_{ik}(\mathbf{x},t) a_{kj}(\mathbf{x},t) = -\frac{\partial p}{\partial X_i \partial X_j} + \nu \frac{\partial^2 a_{ij}(\mathbf{X},t)}{\partial X_k \partial X_k}. \quad (2.16)$$

As mentioned in the introduction, we do not consider the effect of anisotropic pressure-Hessian in this work. If we neglect the anisotropic part of pressure Hessian, we have

$$\frac{\partial^2 p}{\partial X_i \partial X_j} = -\frac{1}{3} a_{nm}(\mathbf{x},t) a_{nm}(\mathbf{x},t) \delta_{ij}. \quad (2.17)$$

In equations (2.16) and (2.17), the spatial derivatives are still evaluated in Eulerian frame (present configuration). The viscous diffusion term can be rewritten in terms of the Lagrangian derivatives (reference configuration) : to leading order, we have

$$\nu \frac{\partial^2 a_{ij}(\mathbf{X},t)}{\partial X_k \partial X_k} \approx \nu \frac{\partial x_m}{\partial X_k} \frac{\partial x_n}{\partial X_k} \frac{\partial^2 a_{ij}(\mathbf{x},t)}{\partial x_m \partial x_n} = \nu C_{mk} C_{nk} \frac{\partial^2 a_{ij}(\mathbf{x},t)}{\partial x_m \partial x_n}, \quad (2.18)$$

where $C_{ij} = \partial x_i / \partial X_j$. The transformation tensor C_{ij} represents the deformation experienced by a fluid particle relative to its original state at time $t = 0$. Then, the velocity gradient

evolution equation becomes

$$\frac{d}{dt}a_{ij}(\mathbf{x},t) + a_{ik}(\mathbf{x},t)a_{kj}(\mathbf{x},t) - \frac{1}{3}a_{mn}(\mathbf{x},t)a_{nm}(\mathbf{x},t)\delta_{ij} \approx \nu C_{mk}C_{nk} \frac{\partial^2 a_{ij}(\mathbf{x},t)}{\partial x_m \partial x_n}. \quad (2.19)$$

In the above equation, all the derivatives are taken with respect to the Lagrangian coordinate system. The effect of the velocity gradient time history on viscous action is contained in the Cauchy-Green tensor $C_{mk}C_{nk}$. In the field of continuum mechanics, the Cauchy-Green tensor is widely used to describe material element deformation. This Cauchy-Green tensor provides gradient (distance) information in the present (Eulerian) configuration. When viewed from the reference (Lagrangian) coordinate frame, the effect of the velocity field is to steepen present configuration gradients and render the effective viscosity ($\nu C_{mk}C_{nk}$) enhanced and anisotropic.

In this work, we will focus only on the increased viscosity magnitude. We set

$$C_{mk}C_{nk} \approx \frac{1}{3}\delta_{mn}C_{pq}C_{pq}, \quad (2.20)$$

leading to

$$\frac{d}{dt}a_{ij}(\mathbf{x},t) + a_{ik}(\mathbf{x},t)a_{kj}(\mathbf{x},t) - \frac{1}{3}a_{mn}(\mathbf{x},t)a_{nm}(\mathbf{x},t)\delta_{ij} = \frac{\nu}{3}C_{pq}C_{pq} \frac{\partial^2 a_{ij}(\mathbf{x},t)}{\partial x_k \partial x_k}. \quad (2.21)$$

Here, $\nu C_{pq}C_{pq}/3 \equiv \nu_T$ can be interpreted as the effective turbulent viscosity. It is shown in Girimaji¹³ that $C_{pq}C_{pq}$ grows exponentially at long times :

$$C_{pq}C_{pq} \sim \exp((a_1 + a_2)t), \text{ where } a_1 + a_2 > 0. \quad (2.22)$$

Thus for fluid particles with large velocity gradients, effective viscosity will be very large (growing exponentially fast) keeping the gradients bounded. This physical picture is consistent with the velocity gradient behavior in turbulence. It is also known that the distribution of $C_{pq}C_{pq}$ is nearly lognormal with long tails indicating intermittent character.

As a modeling hypothesis, we propose that the intermittent character of the viscous relaxation timescale is entirely due to the viscosity enhancement factor $C_{pq}C_{pq}$. We note that the Lagrangian field is not directly affected by the velocity field. Hence, it is reasonable to expect the behavior of $\nu \partial^2 a_{ij} / \partial x_k \partial x_k$ to be similar to that in pure diffusion case (in the absence of velocity field) so that it is characterized by a constant relaxation time-scale. Thus,

$$\nu \frac{\partial^2 a_{ij}(\mathbf{x}, t)}{\partial x_k \partial x_k} \approx \left\langle \nu \frac{\partial^2 Y}{\partial x_k \partial x_k} \Big| Y = a_{ij}(\mathbf{x}, t) \right\rangle \approx -\frac{1}{\tau_L} a_{ij} \quad (2.23)$$

where τ_L is a constant, to be interpreted as the molecular viscous relaxation time-scale. The molecular viscous relaxation time-scale is inversely proportional to the molecular viscosity ($\tau_L \sim 1/\nu$). So, the overall model for viscous effects is

$$\nu \frac{\partial^2 a_{ij}}{\partial X_k \partial X_k} \approx \frac{\nu}{3} C_{pq} C_{pq} \frac{\partial^2 a_{ij}}{\partial x_k \partial x_k} \approx -\frac{C_{pq} C_{pq}}{3\tau_L} a_{ij}. \quad (2.24)$$

The model is effectively a Lagrangian linear diffusion model (LLDM) with a viscosity enhancement factor $C_{pq}C_{pq}$. In the light of equation (2.24), the original LDM can be regarded as a constant Eulerian relaxation time-scale model. With current model, the Eulerian relaxation time-scale is given by

$$\tau_E = \frac{3\tau_L}{C_{pq} C_{pq}} \quad (2.25)$$

where $C_{pq}C_{pq}$ is a function of time history of velocity gradient. In a turbulent flow, the maximum value of effective viscosity and the minimum value of effective relaxation time scale are limited by their corresponding Kolmogorov-scale values, i.e.,

$$(\nu_T)_{max} = \nu_K \sim u\eta; \quad (\tau_E)_{min} = \tau_K \sim \frac{\eta}{u} = \frac{\eta^2}{\nu} \quad (2.26)$$

where η and u are Kolmogorov length and velocity scales respectively. The modeled

time-scale must also satisfy this bound. Thus, the complete model for the relaxation time-scale is

$$\tau_E = \min\left(\frac{3\tau_L}{C_{pq} C_{pq}}, \tau_K\right) \quad (2.27)$$

where $\tau_L = L^2 / \nu$ and L is the integral length scale of turbulence. The model relaxation time-scale value ranges from the near-laminar (molecular) value to the Kolmogorov-scale value as is the case in Navier-Stokes turbulence. In summary, the effective viscosity depends on the molecular viscosity and the ability of turbulence to steepen velocity gradients. This is clearly consistent with the prevailing qualitative picture of viscous action in turbulent flow fields.

To complete the model specification, an appropriate closure for C_{ij} must be found in terms of velocity-gradients. In fact, an accurate representation of C_{ij} is crucial for the success of the model since it contains the information about deformation history. Fortunately, the evolution of C_{ij} depends only on the velocity-gradients. From the equation (2.14), we can write

$$\frac{d}{dt}\left(\frac{\partial X_i}{\partial x_j}\right) = \frac{\partial u_i}{\partial x_j} = \frac{\partial u_i}{\partial X_k} \frac{\partial X_k}{\partial x_j} = a_{ik} \frac{\partial X_k}{\partial x_j}. \quad (2.28)$$

The deformation tensor C_{ij} is the inverse of $\partial X_i / \partial x_j$ and solving the above equation is equivalent to solving an evolution equation for C_{ij} . Thus, the viscous effect can be completely described without any further closure assumptions. This is an important positive feature of the proposed viscous-effect model.

2.3.2 Effect of forcing

In order to sustain a statistically stationary isotropic velocity field, low

wavenumbers are forced in a typical DNS calculation. It is important to account for the effect of this forcing on the velocity gradient evolution to perform an accurate comparison with DNS data. Three popular techniques for sustaining stationary isotropic turbulence are (i) stochastic isotropic forcing of low-wavenumbers, (ii) holding the amplitude of low-wavenumbers constant while permitting change in their phase and, (iii) assigning negative viscosity to low-wavenumbers. While the exact nature of the forcing certainly affects the turbulence large-scales, it is reasonable to argue that high-wavenumbers are relatively insensitive to the method of forcing. Therefore, for the sake of simplicity, we account for the effect of forcing with a linear forcing model. The forced model equation is

$$\frac{da_{ij}}{dt} = -a_{ik}a_{kj} + \frac{1}{3}a_{mn}a_{nm}\delta_{ij} - \frac{C_{pq}C_{pq}}{3\tau_L} \left(1 - \frac{\varepsilon_s}{\varepsilon}\right) a_{ij}; \quad \varepsilon \equiv a_{ij}a_{ij} \quad (2.29)$$

where ε_s is a pre-assigned value for each fluid-particle. Such forcing ensures that the value of $a_{ij}a_{ij}$ of a fluid-particle tends to ε_s at long times. One of the main motivations of choosing this form of forcing is that the probability density function (PDF) of $a_{ij}a_{ij}$ will tend to that of ε_s . Thus, by prescribing the required PDF for ε_s , any desired distribution of $a_{ij}a_{ij}$ can be obtained.

In this model, the time-scale of the linear forcing is chosen to be identical to that of viscous action. This is easy to justify, since the rate of energy input into the system must match the loss due to viscous action. Thus, the forcing process is controlled by viscous process. On the whole, the viscous and forcing processes are controlled by the parameter τ_L . The value of τ_L clearly will depend on the Reynolds number of the flow of interest. However, the precise value of τ_L is irrelevant so long as $\tau_L^{-1} \ll \langle a_{ij}a_{ij} \rangle^{1/2}$ or $\tau_L^{-1} \ll (\varepsilon_s)^{1/2}$. This again is consistent with the physical picture that turbulence is

somewhat insensitive to Reynolds number provided that it is high enough. In all the problems considered in this research, $\tau_L=1$ whereas $\langle \varepsilon_s \rangle \approx 150$. Other choices of τ_L make only qualitative difference in the results obtained.

2.3.3 Numerics

The time evolution of the velocity gradient of each particle is obtained numerically by integrating equations (2.26) and (2.29) using 4th-order Runge-Kutta method. In the simulations, a_{ij} and ε_s values of different fluid particles are assigned from DNS data¹⁴. Depending on the quantity of interest, 3,000 to 30,000 fluid elements are used in the model calculations. The results are summarized in the next section.

2.4 RESULT AND DISCUSSION

We will now investigate the turbulence small scale-structure predicted by the various models and their behavior in decaying and forced isotropic turbulence. The DNS data of forced isotropic turbulence used for comparison here are those of Yeung¹⁴ ($Re_\lambda=90$) and Martin et. al⁷ ($Re_\lambda=40$).

2.4.1 Small-scale geometry

Direct numerical simulations have revealed some universal aspects of the turbulence small-scale structure : (i) the intermediate eigenvalue (a_2) of the strain-rate tensor is mostly positive; (ii) the vorticity vector is aligned along this intermediate eigenvector with a high probability. As shown by Viellefosse¹¹ and Cantwell³, the restricted Euler model captures these features. It is important that the viscous effects model also retains this velocity gradient structure. To investigate the internal geometry

of the new model, we define normalized velocity gradient tensor and time as

$$b_{ij} = a_{ij} / \sqrt{a_{mn} a_{mn}} = \tau' a_{ij}; \quad dt' = dt / \tau'; \quad \tau' = 1 / \sqrt{a_{mn} a_{mn}}. \quad (2.30)$$

Using equation (2.5), we can derive the evolution equations for the normalized quantities :

$$\frac{db_{ij}}{dt'} = -b_{ik} b_{kj} + \frac{1}{3} b_{mn} b_{nm} \delta_{ij} + b_{lm} b_{mn} b_{ln} b_{ij} + \tau'^2 h_{ij} - \tau'^2 b_{mn} h_{mn} b_{ij} \quad (2.31)$$

$$\frac{d\tau'}{dt'} = b_{ij} b_{jk} b_{ik} \tau' - b_{ij} h_{ij} \tau'^3. \quad (2.32)$$

Here, h_{ij} is given by

$$h_{ij} = \begin{cases} 0 & , \text{ restricted Euler} \\ -(1/\tau_E)(b_{ij}/\tau') & , \text{ LDM} \\ -(C_{pq} C_{pq} / 3\tau_L)(b_{ij}/\tau') & , \text{ LLDM} \end{cases}. \quad (2.33)$$

Equations (2.31) and (2.32) respectively govern the geometry and the magnitude of velocity gradients. The evolution of the magnitude of the velocity gradient (or invariants R and Q) is totally different for each model. However, the last two terms in equation (2.31) cancel each other for both LDM and LLDM (recall, $b_{ij} b_{ij} = 1$) rendering the normalized velocity gradient tensor geometry identical for the restricted-Euler model, LDM and LLDM. This means that LDM and LLDM retain all of the geometrical characteristics of the velocity gradient tensor incumbent in the restricted-Euler model.

2.4.2 Unforced isotropic turbulence

According to Navier-Stokes physics, an unforced turbulent velocity field will dissipate all its energy leading at long times to $a_{ij} = 0$. In this respect, restricted-Euler model and LDM are far from describing real physics of the velocity gradient field. In the restricted-Euler model, there is only one fixed point ($R=0, Q=0$), which is not attracting.

As shown in Figure 2.1, the velocity gradients diverge in finite time along the constant discriminant line on (R, Q) phase plane. In case of LDM, the convergence of the velocity gradient depends on its initial value (Figure 2.2, $\tau_E=1$). There exist two fixed points $(R=0, Q=0)$ and $(R=2/\tau_E^2, Q=-3/\tau_E^3)$ which are stable node (local attractor) and saddle (non-attractor) respectively. As pointed out by Martin et. al⁸, LDM is physical only for small to moderate values of the invariants (or velocity gradients) when the trajectory is attracted to $(R=0, Q=0)$. The present LLDM has one fixed point (at $R=0, Q=0$) which is a stable node (global attractor). Results from the LLDM simulations are shown in Figure 2.3. For the sake of comparison, the same initial values have been used as for restricted-Euler model and LDM (Figures 2.1 and 2.2). As required, all the LLDM velocity gradient trajectories are attracted to the origin in (R, Q) phase plane irrespective of the initial conditions. The observed behavior can be readily explained by inspection of equation (2.21), (2.22) and (2.24). Any increase in a_{ij} results in a rapid increase in the effective viscosity through an increase in C_{ij} curbing further growth of velocity-gradients. This characteristic of LLDM is consistent with the Navier-Stokes physics in which a high value of velocity gradient is associated with a smaller relaxation time-scale causing the velocity gradient to remain bounded.

2.4.3 Forced isotropic turbulence

Behavior of invariants

We will now compare the behavior of the LLDM in forced isotropic turbulence against DNS data. Figure 2.4 is a typical scatter plot of invariants R and Q obtained from DNS data. This figure shows that the invariants are concentrated near the origin of (R, Q) plane in significant numbers. This corresponds to purely sheared fluctuations. A

secondary tendency of turbulence is that invariants are densely distributed near the right branch of $D=0$ curve. Near this branch, the evolution of invariants is very slow suggesting that the right branch of the $D=0$ curve is an attracting manifold in (R, Q) phase space⁹. Figure 2.5 shows the (R, Q) steady-state scatter plot from a forced LLDM calculation. The velocity gradients corresponding to Figure 2.4 are used as initial values. For linearly forced LLDM, h_{ij} can be written as

$$h_{ij} = -\frac{C_{pq}C_{pq}}{3\tau_L} \left(1 - \frac{\varepsilon_s}{\varepsilon}\right) a_{ij}. \quad (2.34)$$

From equation (2.8) and (2.9), we derive the evolution equation of the discriminant :

$$\frac{dD}{dt} = -6 \frac{C_{pq}C_{pq}}{3\tau_L} \left(1 - \frac{\varepsilon_s}{\varepsilon}\right) D. \quad (2.35)$$

From this equation, we deduce the behavior of the forced LLDM in isotropic turbulence as follows. Initially, the system behaves like the restricted-Euler model. At steady state, ε converges to ε_s and D goes to zero. As a result, all particles cluster near $D=0$ branch. The clustering is more dense in the fourth quadrant of the (R, Q) plane because of the character of the non-linear term which is the dominant feature of the original restricted Euler equation. Thus, the current model results are consistent with those of DNS observation (Figure 2.5). The R and Q distributions do not even attain a statistically stationary state in restricted-Euler model and LDM calculation. For this reason, the original restricted-Euler model and LDM are quite unphysical making even simple comparison with DNS data virtually impossible. The LLDM must therefore be considered physically most accurate as it does yield a statistically stationary state that is reasonably close to DNS data. For even better agreement, effect of anisotropic pressure Hessian must be accounted for.

Small-scale statistics

The forced LLDM equation (2.28) is devised to yield any specified ε -PDF (probability density function) by suitably choosing the values of ε_s . However, behavior of the PDFs' of other variables predicted by the model is not known. We will now compare the PDFs' of the viscous diffusion terms of a_{ij} , s_{ij} and ω_i obtained from forced LLDM with DNS results. The model results are shown in Figure 2.6. Comparison with the similar PDFs' of DNS data presented in Ref. 7 (Figure 1) reveals that the LLDM captures all the qualitative features, especially near log-normality of the distributions quite well. The quantity that most accurately reflects the viscous action of the model is the conditional average of the viscous diffusion term. It is defined as $\langle \nu \partial^2 Y / \partial X_i \partial X_i | Y \rangle$, where Y is any variable of interest. According to the LLDM, the conditional average of the viscous diffusion term is given by

$$\left\langle \nu \frac{\partial^2 Y}{\partial X_i \partial X_i} \middle| Y \right\rangle \approx - \left\langle \frac{C_{pq} C_{pq}}{3\tau_L} \middle| Y \right\rangle Y = - \left\langle \frac{1}{\tau_E} \middle| Y \right\rangle Y \quad (2.36)$$

where $Y = a_{ij}$, s_{ij} or ω_i . The conditional averages from forced LLDM calculation are shown in Figure 2.7. In this plot, the slope of the curve at a given value of the variable represents the inverse of conditional averaged Eulerian viscous relaxation time-scale. Referring to the plot of the same quantity calculated from DNS data (Ref.7, Figure 2), we can conclude that the LLDM reproduces the qualitative features of the conditional diffusion quite well and the quantitative aspects reasonably adequately.

2.5 CONCLUSION

In order to accurately describe velocity-gradient dynamics in a turbulent flow field, the restricted-Euler model must be augmented with adequate models for

anisotropic pressure Hessian and viscous effects. Of these two, accounting for the viscous effects is particularly important to prevent finite time divergence of the model equations. In this research, a new model - Lagrangian linear diffusion model (LLDM) - is proposed to account for viscous effects. Using Lagrangian reference frame analysis, a variable viscous relaxation time-scale model is derived. Consistent with Navier-Stokes physics, the viscous relaxation time-scale experienced by a fluid element depends on its deformation history. The model relaxation time-scale ranges from near-laminar values to Kolmogorov-scale value. A simple model for forcing model is also introduced for the purpose of clean comparison of the model results with forced isotropic turbulence DNS data. Analysis reveals that LLDM retains all the geometrical characteristics of the velocity gradient tensor inherent in the restricted-Euler model. Very importantly, RE-LLDM equation (restricted-Euler equation with LLDM viscous model) does not diverge and, therefore, it can be used as a quantitative model for velocity gradient dynamics. The PDFs' and conditional average of the viscous diffusion terms of various quantities - a_{ij} , s_{ij} and ω_i - predicted by the model compare well with DNS data. It must be pointed out that similar comparison with previous models is not possible because the predicted velocity-gradients diverge in finite time.

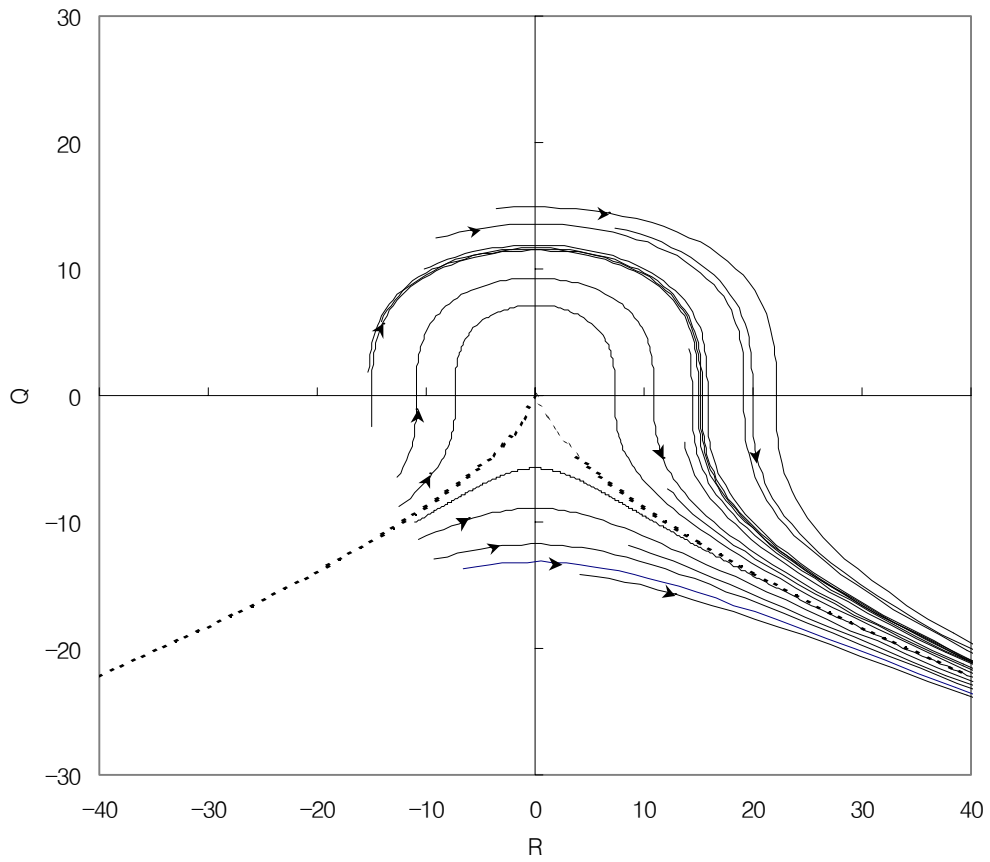


Figure 2.1 Typical R - Q trajectory of the restricted-Euler model. Dotted line represents $D = 27R^2 / 4 + Q^3 = 0$.

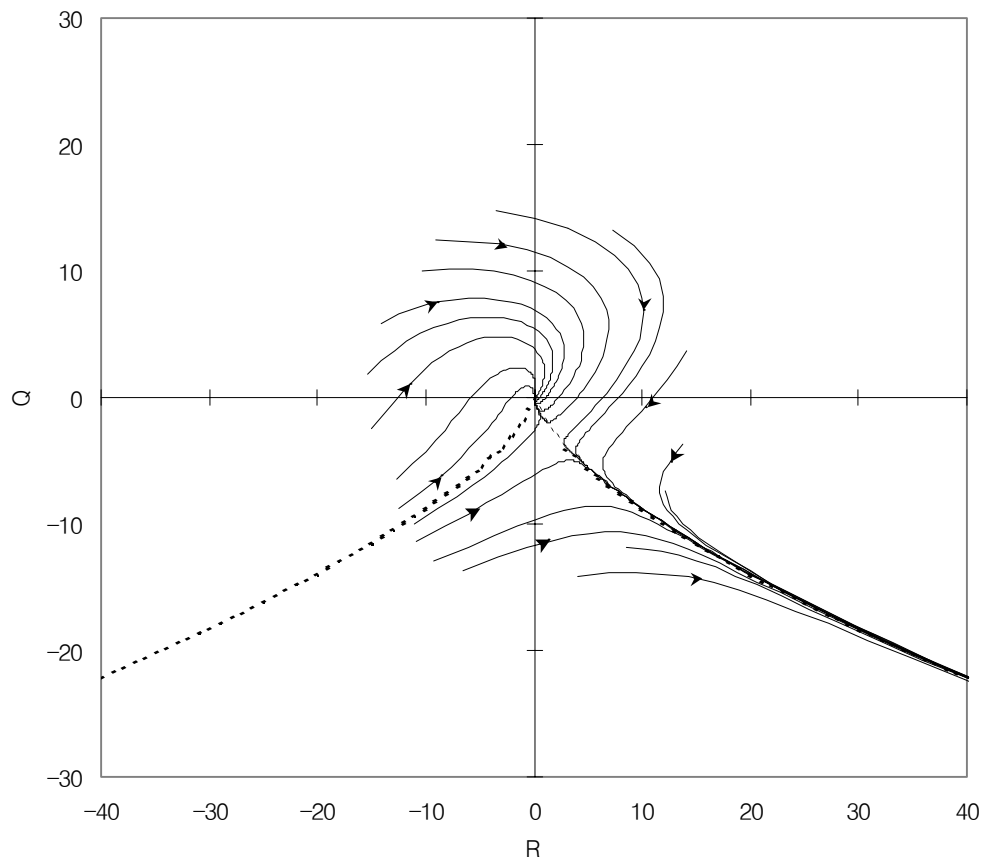


Figure 2.2 Typical R - Q trajectory of the LDM.

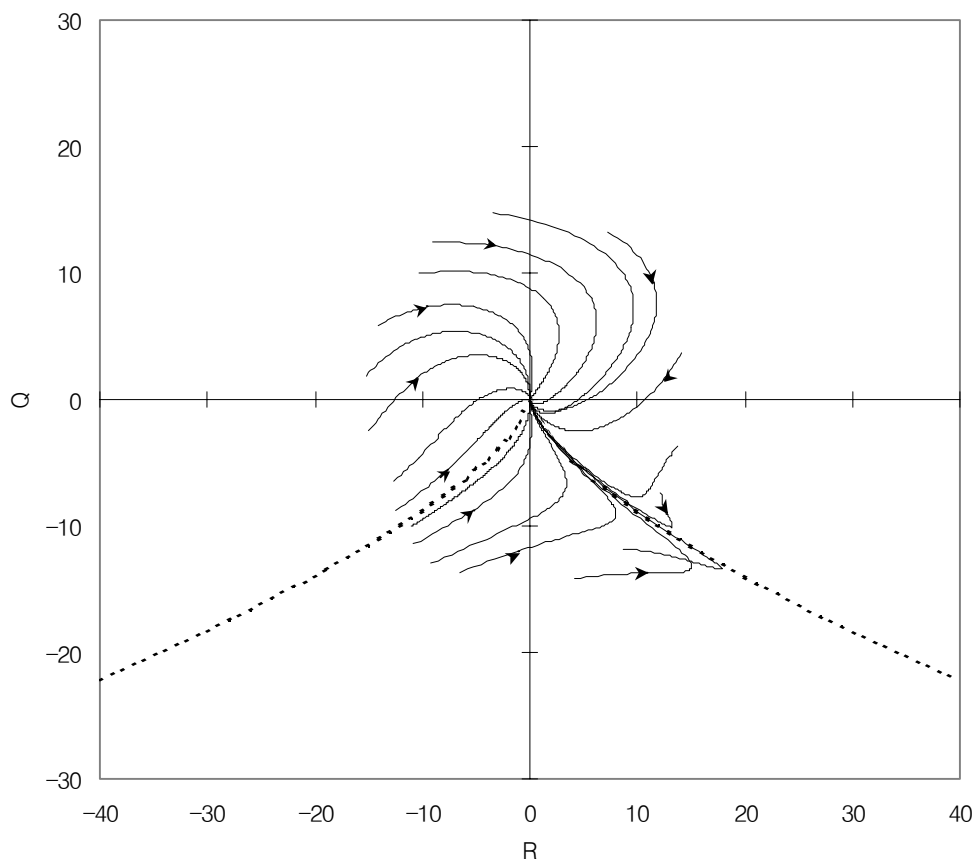


Figure 2.3 Typical R - Q trajectory of the LLDM.

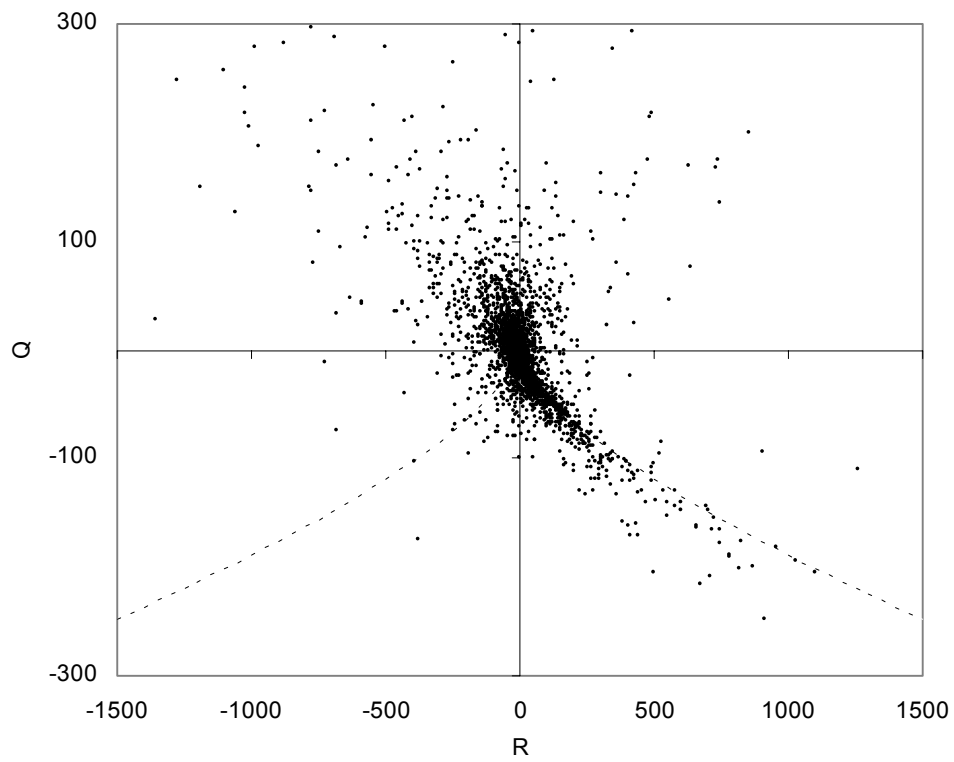


Figure 2.4 R - Q scatter plot of DNS result for isotropic turbulence with small wave-number forcing ($Re_\lambda=90$, Yeung¹⁴).

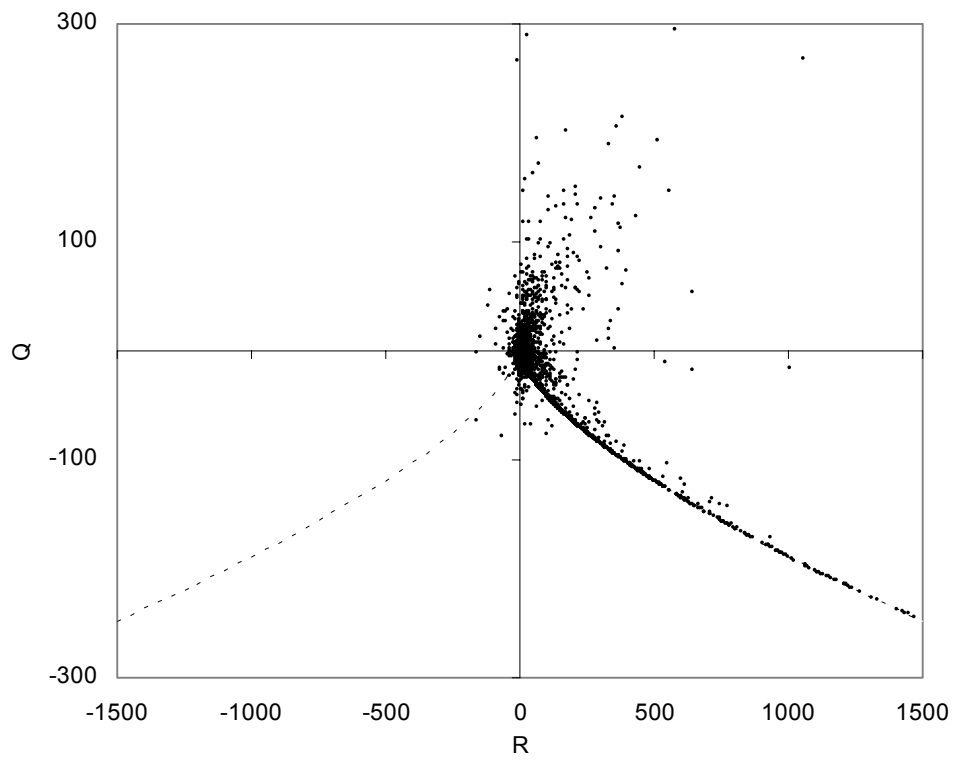


Figure 2.5 R - Q scatter plot of forced LLDM at nearly steady state.

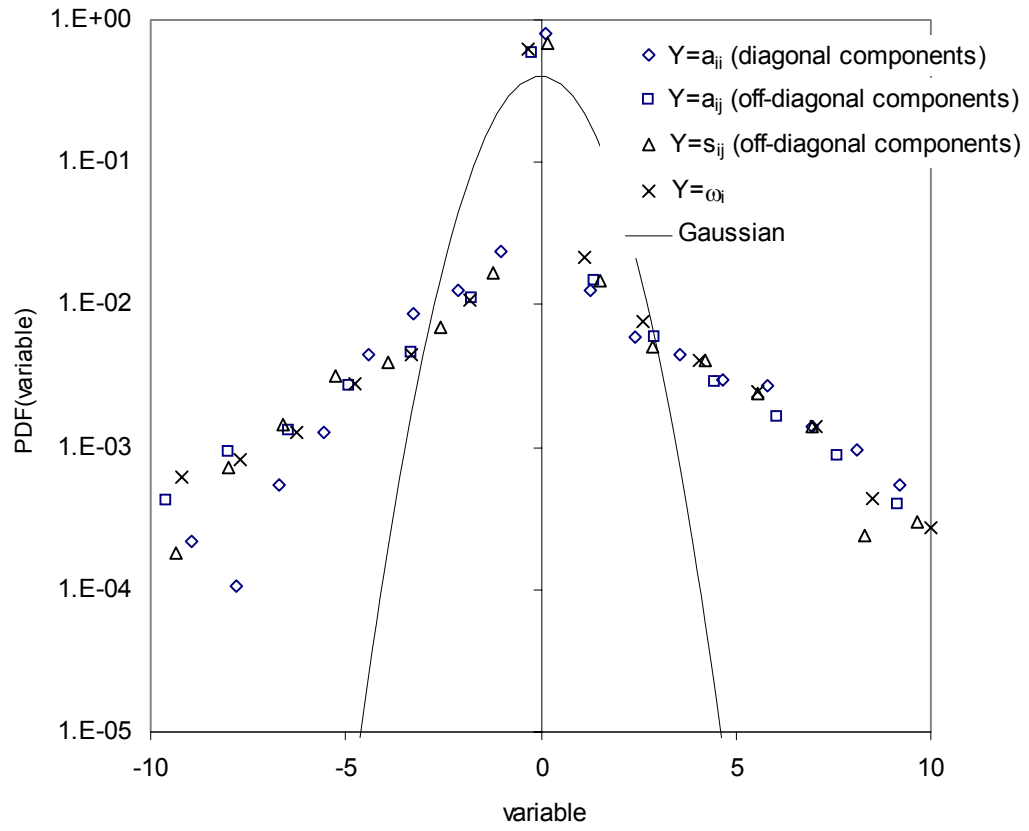


Figure 2.6 Normalized probability density functions of viscous diffusion terms in forced LLDM. Variable= $\nu \nabla^2 Y / \sigma(\nu \nabla^2 Y) = (-C_{pq} C_{pq} Y / 3\tau_L) / \sigma(-C_{pq} C_{pq} Y / 3\tau_L)$.
 σ = standard deviation. $Y = a_{ij}, s_{ij}$ or ω_i .

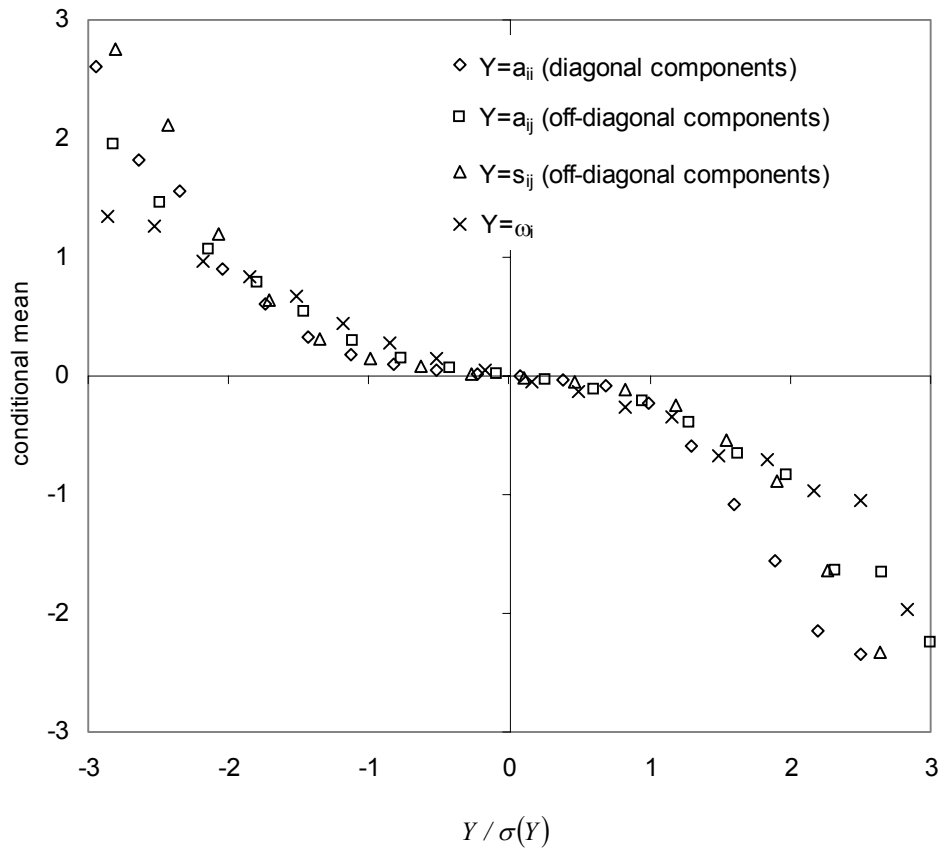


Figure 2.7 Plot of conditional average of viscous diffusion versus corresponding variables in forced LLDM. Conditional mean = $\langle \nu \nabla^2 Y | Y \rangle / \sigma(\nu \nabla^2 Y)$, equation (2.36). $Y = a_{ij}, s_{ij}$ or ω_i .

CHAPTER III

PRESSURE-STRAIN CORRELATION IN HOMOGENEOUS ANISOTROPIC TURBULENCE SUBJECT TO RAPID STRAIN- DOMINATED DISTORTION

In this chapter, the second topic, “pressure-strain correlation in homogeneous anisotropic turbulence subject to rapid strain-dominated distortion” is investigated. For the better understanding of the physics of the pressure-strain correlation in strain-dominated mean flows, rapid distortion calculations are performed with various anisotropic turbulence initial conditions. Based on the results of simulations, we infer important physical characteristics of the “rapid” pressure-strain correlation $\Phi_{ij}^{(r)}$ in such flows: i) it vanishes when there is no production of anisotropy, ii) in the proximity of two-componential state it tends to decrease Reynolds stress anisotropy, and iii) its magnitude is generally smaller than that of production. The observed characteristics are proposed as criteria that pressure-strain correlation models may be required to satisfy. All of the current popular models violate the above criteria for a sizeable subset of anisotropic initial conditions. Reynolds stress transport model calculations show that unphysical and unrealizable model behavior can be directly attributed to these violations

3.1 INTRODUCTION

Accurate modeling of the pressure-strain correlation is one of the most important challenges in the second-moment turbulence closure model. In particular, the “rapid” portion of the pressure-strain correlation has been the subject of many analytical and

modeling studies. When turbulence is subjected to rapid distortion (RD), its evolution is simply described by so-called rapid-distortion theory (RDT). The RDT equation is linear in fluctuating velocity. In RD limit, the physics of rapid pressure-strain correlation can be studied in isolation because complicate effects of slow pressure-strain correlation and dissipation are absent. Another important feature of this limit is that the fluid behaves as an elastic material rather than viscous medium. The stresses and other turbulence properties including the pressure-strain correlation depend on the total strain (deformation) experienced by the fluid element rather than the current strain rate.

In homogeneous turbulence, the rapid pressure-strain correlation can be expressed as a function of the velocity spectrum tensor¹⁵. In RDT, which is a multi-point description of turbulence, the pressure-strain correlation appears in closed form as the velocity spectrum is fully known. To describe accurately the pressure-strain correlation at the one-point closure level, at a minimum two independent turbulence field tensors - componentality and dimensionality - are needed^{16,17}. In the traditional second-moment closure approach, the Reynolds stress tensor contains the componentality information while dimensionality tensor is not known. Depending on the dimensionality tensor, the pressure-strain correlation takes a large range of values for a given combination of Reynolds stresses and the mean velocity field¹⁷. Thus, without the knowledge of the dimensionality tensor, the problem of the rapid pressure-strain correlation closure is not well-posed and the solution is not unique.

The challenge of traditional one-point closure modeling is to select a single appropriate value for the pressure-strain correlation within the range of allowable values for the given Reynolds stress tensor. Given this limitation, no single one-point closure model can simulate the entire range of physics incumbent in the RDT equations. This leads to the question, how can RDT solutions be used to improve one-point closure

models? The best that can be expected of any general traditional one-point closure model is that it embodies the most likely features of the RDT solutions: features that are common for the largest set of dimensionality tensors for a given Reynolds stress tensor. As a result, in one-point closure modeling, many of the pathological aspects of the RDT behavior will have to be excluded in favor of the dominant highly-probable features.

In this research, we will address only those modeling issues that pertain to fundamental consistency with RDT physics and realizability matters. The focus is on physics of pressure-strain correlation in rapidly-distorted homogeneous anisotropic turbulence, where our understanding is relatively poor. Specifically, we study extreme cases of initial turbulence anisotropy: two-component (2C) and one-component (1C) turbulence, along with isotropic turbulence. This choice is motivated by the argument that if rapidly-distorted turbulence behavior can be well understood and modeled at the three extremes of the Lumley invariant triangle map¹⁸, the behavior at any arbitrary level of anisotropy can, perhaps, be inferred.

Several types of strain-dominated rapid deformation - homogeneous shear (HS), plain strain (PS), axisymmetric contraction (AC), and axisymmetric expansion (AE) - are considered in this study. Once some degree of understanding of the rapid pressure-strain correlation physics is developed, we will attempt to formulate general guidelines to aid in future model developments. The model guidelines derived in the research are expressly for strain-dominated mean flows. Rotation-dominated (elliptic) mean flows and flow in rotating frames will be examined in a separate study as the behavior of these flows in the RD limit significantly differs from that of strain-dominated flows. Girimaji¹⁹ demonstrates that coefficients in a rapid pressure-strain correlation model must depend upon the mean flow in order to accurately capture turbulence physics. Therefore, it is logical to postulate different guidelines for different mean flows.

The objectives of the present study are: i) to develop a better understanding of the pressure-strain correlation in highly anisotropic turbulence subject to rapid strain-dominated distortion; ii) to assess model performance (physical consistency, realizability) by comparison with RDT data; iii) to seek physical principles and mathematical constraints, which can be used to guide development of better pressure-strain correlation models in the RD limit for anisotropic turbulence; iv) to estimate bounds on the values of the pressure-strain correlation.

3.1.1 Background

Isotropic turbulence

As a prelude to the study of initially anisotropic turbulence, we will briefly review the most prominent RDT result in initially isotropic turbulence. Simple analysis shows that pressure-strain correlation can be written in rapidly distorted isotropic turbulence as¹⁵:

$$\Phi_{ij}^{(r)} = \frac{4}{5}kS_{ij} = -\frac{3}{5}\left(P_{ij} - \frac{2}{3}P\delta_{ij}\right), \quad (3.1)$$

where

$$\Phi_{ij}^{(r)} = -\left\langle p^{(r)}(u_{i,j} + u_{j,i}) \right\rangle;$$

$$S_{ij} = \frac{1}{2}\left(\frac{\partial U_i}{\partial x_j} + \frac{\partial U_j}{\partial x_i}\right), P_{ij} = -\langle u_i u_k \rangle \frac{\partial U_j}{\partial x_k} - \langle u_j u_k \rangle \frac{\partial U_i}{\partial x_k}.$$

In the above: $\Phi_{ij}^{(r)}$ is the “rapid” part of the pressure-strain correlation; $p^{(r)}$ is the “rapid” part of the pressure fluctuation; U_i and u_i are mean and fluctuating velocities components; $k=\langle u_i u_i \rangle/2$ is the turbulent kinetic energy; P_{ij} is the production tensor; $P=P_{ii}/2$; and δ_{ij} is the Kronecker delta symbol. Equation (3.1) is called the Crow

constraint and its use in pressure-strain correlation modeling can be traced to Rotta²⁰. Currently, coefficients in pressure-strain correlation models are chosen to satisfy (3.1) at the RD limit irrespective of the componentality or the dimensionality of turbulence.

Although the result in equation (3.1) has long been known, it is not often recognized that the derivation tacitly assumes that both componentality and dimensionality tensors are isotropic. It is possible to fabricate a turbulent velocity field with an isotropic Reynolds stress (componentality) tensor but an anisotropic dimensionality tensor. Such a velocity field will not satisfy equation (3.1). Thus, even for flows with initially isotropic Reynolds stresses, the Crow constraint is more a modeling guideline than a rigorous mathematical constraint. Yet, this guideline has proved to be quite adequate for all dimensionality tensors provided the componentality tensor is reasonably close to isotropic.

For initially anisotropic turbulence, a model based on the Crow constraint can yield completely unphysical results, as will be shown later. As rapidly-distorted anisotropic turbulence is of great practical interest, it is important to develop modeling guidelines similar to equation (3.1) for anisotropic turbulence.

Anisotropic turbulence

A review of previous anisotropic rapid-distortion studies is given in Hunt and Carruthers²¹. Sreenivasan and Narasimha²² and Maxey²³ (and references therein) investigated the influence of various types of distortion and anisotropy levels on turbulence evolution. In their studies, only special cases of the initial energy spectrum tensor were considered. Various cases of three-component (3C) axisymmetric turbulence, with the Reynolds stress component along the axis of symmetry increasing from its isotropic value of $2/3k$ to the maximum allowed value of k , were studied. Maxey²³

investigated, in some detail, the role of the pressure-strain correlation at the rapid distortion limit and the performance of the model of Launder *et al.*²⁴ in the homogeneous shear flow. Hunt & Carruthers²¹ further pointed out that the asymptotic values of Reynolds stresses depend on the initial anisotropy level. An important conclusion from all these studies is that the level of initial anisotropy plays a crucial role in the subsequent turbulence evolution. However, these studies stop well short of developing general modeling constraints or guidelines in rapidly distorted anisotropic turbulence.

Our first objective is similar to that of previous studies mentioned above. Then, we proceed further to characterize important physical features of pressure-strain correlation and establish new modeling guidelines in anisotropic turbulence.

3.2 GOVERNING EQUATIONS

The velocity fluctuation evolution equations in the RD limit are the following (see, *e.g.*, Pope²⁵)

$$\frac{\overline{D}u_j}{\overline{D}t} = -u_i \frac{\partial U_j}{\partial x_i} - \frac{1}{\rho} \frac{\partial p^{(r)}}{\partial x_j}; \quad \frac{\partial u_i}{\partial x_i} = 0; \quad \frac{1}{\rho} \nabla^2 p^{(r)} = -2 \frac{\partial U_i}{\partial x_j} \frac{\partial u_j}{\partial x_i}. \quad (3.2)$$

Here, $\overline{D}/\overline{D}t = \partial/\partial t + U_i \partial/\partial x_i$. The equations are written in Cartesian coordinates. In homogeneous turbulence, the velocity and the pressure fields can be written in terms of their Fourier components:

$$u_i(\vec{x}, t) = \sum_{\vec{k}} \hat{u}_i(t) e^{i\vec{k}(t)\cdot\vec{x}}, \quad p^{(r)}(\vec{x}, t) = \sum_{\vec{k}} \hat{p}(t) e^{i\vec{k}(t)\cdot\vec{x}}, \quad (3.3)$$

where, $\vec{k}(t)$ is the wavenumber vector and $\hat{u}_i(\vec{k}, t)$ is the Fourier coefficient vector of the velocity fluctuation. Then, equation (3.2) transform to the evolution equations for the components of vectors $\vec{k}(t)$ and $\hat{u}(t)$

$$\frac{d\kappa_j}{dt} = -\kappa_l \frac{\partial U_l}{\partial x_j}, \quad (3.4)$$

$$\frac{d\hat{u}_j}{dt} = -\hat{u}_k \frac{\partial U_l}{\partial x_k} \left(\delta_{jl} - 2 \frac{\kappa_j \kappa_l}{\kappa^2} \right) \quad (3.5)$$

subject to the incompressibility condition:

$$\hat{u}_i \kappa_i = 0. \quad (3.6)$$

Cambon and Scott²⁶ refer equations (3.4)-(3.5) as the Kelvin-Townsend equations. For given initial conditions, equations (3.4)-(3.6) can be solved directly. Then, the covariance of two Fourier coefficients

$$\hat{R}_{ij}(\vec{\kappa}, t) = \langle \hat{u}_i^*(\vec{\kappa}, t) \hat{u}_j(\vec{\kappa}, t) \rangle \quad (3.7)$$

can be extracted from the data for each given $\vec{\kappa}(t)$. Summation of (3.7) over all wavenumber vectors gives the Reynolds stress components in the physical space:

$$\langle u_i u_j \rangle = \sum_{\vec{\kappa}} \hat{R}_{ij}(\vec{\kappa}, t). \quad (3.8)$$

Another way to obtain \hat{R}_{ij} and Reynolds stresses is to solve directly the evolution equation for the covariance of two Fourier coefficients of a given wavenumber vector

$$\frac{d\hat{R}_{ij}}{dt} = -\hat{R}_{ik} \frac{\partial U_j}{\partial x_k} - \hat{R}_{jk} \frac{\partial U_i}{\partial x_k} + 2\hat{R}_{ik} \frac{\partial U_l}{\partial x_k} \frac{\kappa_j \kappa_l}{\kappa^2} + 2\hat{R}_{jk} \frac{\partial U_l}{\partial x_k} \frac{\kappa_i \kappa_l}{\kappa^2}, \quad (3.9)$$

which is derived using equation (3.5). Details of the derivation can be found in Pope²⁵ (p. 412), for instance. Now, the continuity equation takes the following form

$$\kappa_i \hat{R}_{ij}(\vec{\kappa}) = \kappa_j \hat{R}_{ij}(\vec{\kappa}) = 0. \quad (3.10)$$

Equation (3.9) is a numerically more efficient alternative to equation (3.5) for calculating Reynolds stresses at the RD limit²⁷ and, hence, has been adopted in this study. Summation of (3.9) over all $\vec{\kappa}(t)$ yields the Reynolds stress evolution equation in the RD limit:

$$\frac{d\langle u_i u_j \rangle}{dt} = P_{ij} + \Phi_{ij}^{(r)}, \quad (3.11)$$

where production P_{ij} is given by

$$P_{ij} = -\sum_{\bar{k}} \left(\hat{R}_{ik} \frac{\partial U_j}{\partial x_k} + \hat{R}_{jk} \frac{\partial U_i}{\partial x_k} \right)$$

and the ‘‘rapid’’ pressure-strain correlation $\Phi_{ij}^{(r)}$ is

$$\Phi_{ij}^{(r)} = 2 \sum_{\bar{k}} \left(\hat{R}_{ik} \frac{\partial U_l}{\partial x_k} \frac{\kappa_j \kappa_l}{\kappa^2} + \hat{R}_{jk} \frac{\partial U_l}{\partial x_k} \frac{\kappa_i \kappa_l}{\kappa^2} \right).$$

Thus, the RDT equations can be used directly to study the physics of production and pressure-strain redistribution processes.

In the current study, RDT data are used to evaluate directly the accuracy of three popular models for the ‘‘rapid’’ part of the pressure-strain correlation - IP (isotropization-of-production) model²⁸, LRR model²⁴, and SSG model²⁹ - for several isotropic and anisotropic initial conditions. Only linear and quasi-linear models are chosen as non-linear models violate one of the basic requirements of rapid pressure-strain correlation closure²⁵. IP, LRR, and SSG models can be represented in the general form:

$$\begin{aligned} \Phi_{ij}^{(r)} = & -C_1^1 P b_{ij} + \left(C_2^0 - C_2^1 \sqrt{b_{kk}^2} \right) k S_{ij} + C_3 k \left(b_{ik} S_{jk} + b_{jk} S_{ik} - \frac{2}{3} b_{kl} S_{kl} \delta_{ij} \right) \\ & + C_4 k \left(b_{ik} W_{jk} + b_{jk} W_{ik} \right) \end{aligned} \quad (3.12)$$

In the above, b_{ij} denotes the anisotropy tensor and W_{ij} is the mean rotation-rate (vorticity) tensor:

$$b_{ij} = \frac{\langle u_i u_j \rangle}{2k} - \frac{1}{3} \delta_{ij} \quad ; \quad W_{ij} = \frac{1}{2} \left(\frac{\partial U_i}{\partial x_j} - \frac{\partial U_j}{\partial x_i} \right).$$

The models differ only in the value of coefficients, which are given in Table 3.1. The value 0.8 of the coefficient C_2^0 recommended in all three models, comes from

constraint (3.1).

3.3 CALCULATION PROCEDURE

The RDT equations ((3.4), (3.9)-(3.10)) and modeled Reynolds stress evolution equation (3.11) are solved in a variety of homogeneous turbulent flows. Mean flows investigated here are *homogeneous shear (HS)*

$$\frac{\partial U_i}{\partial x_j} = \begin{pmatrix} 0 & S & 0 \\ 0 & 0 & 0 \\ 0 & 0 & 0 \end{pmatrix},$$

plain strain (PS)

$$\frac{\partial U_i}{\partial x_j} = \begin{pmatrix} S & 0 & 0 \\ 0 & -S & 0 \\ 0 & 0 & 0 \end{pmatrix},$$

axisymmetric contraction (AC)

$$\frac{\partial U_i}{\partial x_j} = \begin{pmatrix} S & 0 & 0 \\ 0 & -S/2 & 0 \\ 0 & 0 & -S/2 \end{pmatrix},$$

and *axisymmetric expansion (AE)*

$$\frac{\partial U_i}{\partial x_j} = \begin{pmatrix} -2S & 0 & 0 \\ 0 & S & 0 \\ 0 & 0 & S \end{pmatrix}.$$

To describe clearly the initial condition, we introduce two quantities^{16,17} that characterize the velocity spectrum tensor: *componentality (C)* and *dimensionality (D)* of the turbulence field. These are scalars related to the corresponding tensors mentioned in the introduction. *Componentality* refers to the number of non-zero diagonal components in the initial Reynolds stress tensor. *Dimensionality* refers to the number of orthogonal

directions in which wavenumbers are permitted¹⁶. In the present research, turbulence *dimensionality* is always equal to three unless prohibited by incompressibility condition.

In keeping with the main objective of the research, highly anisotropic as well as isotropic turbulent velocity fields are chosen as initial conditions. Anisotropic cases considered are: one-component (1C) and axisymmetric two-component (2C) turbulent states. Three kinds of 1C initial conditions are considered:

$$b_{ij} = \begin{pmatrix} \frac{2}{3} & 0 & 0 \\ 0 & -\frac{1}{3} & 0 \\ 0 & 0 & -\frac{1}{3} \end{pmatrix}; \quad b_{ij} = \begin{pmatrix} -\frac{1}{3} & 0 & 0 \\ 0 & \frac{2}{3} & 0 \\ 0 & 0 & -\frac{1}{3} \end{pmatrix}; \quad b_{ij} = \begin{pmatrix} -\frac{1}{3} & 0 & 0 \\ 0 & -\frac{1}{3} & 0 \\ 0 & 0 & \frac{2}{3} \end{pmatrix}. \quad (3.13)$$

They are denoted as 1C1, 1C2, and 1C3 respectively. The three axisymmetric 2C initial conditions are

$$b_{ij} = \begin{pmatrix} -\frac{1}{3} & 0 & 0 \\ 0 & \frac{1}{6} & 0 \\ 0 & 0 & \frac{1}{6} \end{pmatrix}; \quad b_{ij} = \begin{pmatrix} \frac{1}{6} & 0 & 0 \\ 0 & -\frac{1}{3} & 0 \\ 0 & 0 & \frac{1}{6} \end{pmatrix}; \quad b_{ij} = \begin{pmatrix} \frac{1}{6} & 0 & 0 \\ 0 & \frac{1}{6} & 0 \\ 0 & 0 & -\frac{1}{3} \end{pmatrix}, \quad (3.14)$$

which are denoted as 2C1, 2C2, and 2C3 respectively. Isotropic condition is given by

$$b_{ij} = 0, \quad i, j = 1, 2, 3. \quad (3.15)$$

Values of the anisotropy tensor given in (3.13)-(3.15) are used directly to solve modeled Reynolds stress evolution equation (3.11).

To solve RDT equations (3.4), (3.9), and (3.10), initial turbulence fields with desirable properties should be generated. Since many different choices of the wavenumber vectors and the Fourier coefficients of the velocity fluctuation can yield the required anisotropy, the choice of the initial fields for these quantities must be made

carefully. As was mentioned in the introduction, it is important to choose an initial field that captures the features common to most, if not all, wavenumber distributions (dimensionalities). The clear choice, then, is uniform distributions of wavenumbers and velocity vectors within the range permitted by the initial Reynolds stress tensor. Thus, in the present study the following assumptions on the initial distributions of vectors $\vec{\kappa}(t=0)$ and $\hat{u}(\vec{\kappa}, t=0)$ are made:

- a) Velocity fluctuations in all permissible directions are equally energetic. That is, Fourier coefficients of initial velocity fluctuations in all permissible directions have the equal magnitude. Whether Fourier coefficient vectors are permitted in a specific direction is determined from the initial turbulence componentality;
- b) For a given vector $\hat{u}(t=0)$ all permissible wavenumber vector directions are equally probable. Permissible wavenumber vector directions are determined purely by incompressibility condition (3.6).

Thus, the most general (unbiased) initial velocity field can be generated for the specified Reynolds stress tensor. For 1C turbulence, the initial vector \hat{u} is aligned along the corresponding unit vector. In 2C turbulence, initial vectors \hat{u} are uniformly distributed in a circle on the permissible plane. In 3C isotropic case, vectors \hat{u} are uniformly distributed on a sphere. The magnitudes of \hat{u} are such that the total initial turbulent kinetic energy is recovered.

For each vector $\hat{u}(t=0)$, the corresponding wavenumber vectors $\vec{\kappa}(t=0)$ are determined from assumption (b) above. Because equation (3.9) does not depend on the magnitude of the wavenumber vector, but on its direction only, one can assume, without loss of the generality that all permissible wavenumber vectors are of equal magnitude initially. Thus, to generate initially isotropic turbulence, wavenumber vectors are

distributed evenly on the surface of a unit sphere. In 1C turbulence, vectors $\vec{\kappa}(t)$ are uniformly distributed in the unit circle lying in the plane normal to the initial vector \hat{u} . In 2C turbulence, the generation of vectors $\vec{\kappa}$ is explained below for the case of 2C3 turbulence.

In 2C3 turbulence initial vectors \hat{u} are equally distributed in the plane (1,2) (Fig. 3.1). The corresponding wavenumber vector distribution is dictated by incompressibility condition (assumption b). Effectively, the full set of vectors $\vec{\kappa}$ is divided into families, with each family having the same value of the projection of $\vec{\kappa}$ on axis 3 (Fig. 3.1): $\kappa_3^i = |\kappa| \cos(\theta^{i-1} + d\theta)$, for $i = 2, N$ and $\kappa_3^i = |\kappa|$, for $i = 1$. Here, $|\kappa| = 1$, $\theta^1 = 0$, and $d\theta = \pi / 2(N - 1)$. All families carry equal amount of energy. Then, knowing the number of vectors $\vec{\kappa}$ in each family, one can determine the energy associated with each vector $\vec{\kappa}$ and $\hat{R}_{ij}(\vec{\kappa}, t = 0)$. Vectors $\vec{\kappa}$ in the cases of 2C2 turbulence and 2C1 turbulence are generated in the similar manner.

A fourth-order Runge-Kutta scheme was used for time integration of all equations.

3.4 RESULTS AND DISCUSSION

Results from computations of RDT equations ((3.4), (3.9)-(3.10)) and modeled Reynolds stress evolution equation (3.11) are now presented. The mean flows, the initial conditions, and basic outcomes from the RDT and model calculations are given in Table 3.2. The RDT calculations show evolution of anisotropy level in some cases (denoted by ‘E’) and no evolution in others (‘N’). All isotropic turbulence cases evolve from their initial states. Our RDT data interrogation focuses on the role of the pressure-strain correlation, especially its relation to production. The analysis is centered around the

anisotropy evolution equation at the RD limit:

$$\frac{db_{ij}}{dt} = \frac{1}{2k} \left(P''_{ij} + \Phi_{ij}^{(r)} \right), \quad (3.16)$$

where $P''_{ij} (= P_{ij} - 2Pb_{ij} - 2\delta_{ij}P/3)$ is the production of anisotropy. Also crucial in the analysis is the magnitude of anisotropy, which evolves according to

$$\frac{1}{2} \frac{db_{ij}b_{ij}}{dt} = \frac{1}{2k} \left(P''_{ij} b_{ij} + \Phi_{ij}^{(r)} b_{ij} \right). \quad (3.17)$$

We first investigate if a generalized form of constraint (3.1) is possible for an anisotropic flow, that is, if the pressure-strain correlation merely counteracts certain fraction of the production. In such a case, the pressure-strain correlation could have one of two forms:

$$\Phi_{ij}^{(r)} \propto P''_{ij} \quad \text{or} \quad \Phi_{ij}^{(r)} \propto P'_{ij} \left(= P_{ij} - \frac{2}{3} \delta_{ij} P \right),$$

where the proportionality coefficient in each expression could be a constant or a scalar invariant of the mean velocity gradient tensor. The simplest manner to verify the existence of such a linear relationship would be to compute the following ratios

$$R1 = \frac{\Phi_{ij}^{(r)} \Phi_{ij}^{(r)}}{P''_{ij} P''_{ij}} \quad \text{or} \quad R2 = \frac{\Phi_{ij}^{(r)} \Phi_{ij}^{(r)}}{P'_{ij} P'_{ij}}. \quad (3.18)$$

The first ratio $R1$ in (3.18) is, probably, more justified in anisotropic turbulence considering the form of anisotropy evolution equation (3.16) in the RD limit. In isotropic turbulence, when both componentality and dimensionality tensors are isotropic, we have $R1 = R2 = 0.36$ in accordance with (3.1). The RDT data confirm that the ratio $R1$ is indeed preferable to $R2$ because, at $t=0$, $R1$ shows less variation for different initial flow conditions. Nevertheless, even the initial value of the ratio $R1$ changes from case to case: $R1=1$ for HS (1C2, 2C1) and $R1=0.25$ for HS (2C2), PS (2C1, 2C2, 2C3), AE and AC (2C2, 2C3) flows. Further $R1$ and $R2$ change substantially with turbulence

evolution. Some examples of $R1$ evolution are shown in Fig. 3.2. In none of the cases considered, the ratio $R1$ (and $R2$) is equal to the isotropic value 0.36.

One clear conclusion can be drawn from RDT data: the pressure-strain correlation does more than merely counteract the anisotropy production. In the absence of a unique relationship between the production and pressure-strain correlation, subtler connections are now investigated. One of the main features of the pressure-strain correlation is its redistributive nature. The fact that the pressure-strain correlation term $\Phi^{(r)}_{ij}$ is traceless reveals that it does not alter the total energy. It is generally believed that the pressure-strain correlation removes energy from high-energy components and enhances lower-energy components. In contrast, the production process is believed to increase anisotropy by injecting energy into selected components of the Reynolds stress tensor. The specific issues investigated are the following.

- 1) Can there be redistribution without production? That is, what happens to $\Phi^{(r)}_{ij}$, when $P''_{ij}=0$.
- 2) Does the “rapid” pressure-strain correlation always extract energy from high-energy components and deposit it into low-energy ones? This can be answered by monitoring the sign of $\Phi^{(r)}_{ij}b_{ij}$ (refer to equation (3.17)).
- 3) Can more energy be redistributed than produced in the first place? That is, can the $R1$ (or $R2$) value be greater than unity.

3.4.1 RDT results

Non-evolving cases

The RDT calculations demonstrate that in some cases (denoted by ‘N’ in Table 3.2) turbulence anisotropy does not change from its initial level. In other words, the term db_{ij}/dt on the left side of equation (3.16) is equal to zero for each component of the

anisotropy tensor b_{ij} . It is straightforward to show (see the Appendix A) that in such cases all components of the production term P''_{ij} are exactly equal to zero. It follows then from equation (3.16), that the pressure-strain tensor components should also be equal to zero. Thus, if $P''_{ij}=0$, then $\Phi^{(r)}_{ij}=0$. In order to confirm this, we examine the second invariant of tensors P''_{ij} and $\Phi^{(r)}_{ij}$, i.e., $P''_{ij}P''_{ij}$ and $\Phi^{(r)}_{ij}\Phi^{(r)}_{ij}$. The second invariant contains information about all tensor components. If all individual components of the tensor are equal to zero, so is the invariant. The RDT calculations show that when the invariant $P''_{ij}P''_{ij}$ is equal to zero, then $\Phi^{(r)}_{ij}\Phi^{(r)}_{ij}$ is also equal to zero. Note that in these cases, P_{ij} or P''_{ij} need not vanish.

Evolving cases

Cases in which the RDT predicts turbulence anisotropy evolution are denoted by ‘E’ in Table 3.2. If the pressure-strain correlation decreases anisotropy and the production term increases its level, then $\Phi^{(r)}_{ij}b_{ij}$ in (3.17) should be negative, and $P''_{ij}b_{ij}$ should be positive. The computed RDT values of $P''_{ij}b_{ij}$ and $\Phi^{(r)}_{ij}b_{ij}$ in some representative cases are plotted in Fig. 3.3. The $P''_{ij}b_{ij}$ evolution is shown with a solid line (without symbols), while the $\Phi^{(r)}_{ij}b_{ij}$ evolution is represented by dashed line (without symbols). It is clearly seen that $P''_{ij}b_{ij}$ is always positive as expected, while $\Phi^{(r)}_{ij}b_{ij}$ is predominantly negative (again as expected). In one case (Fig. 3.3e) $\Phi^{(r)}_{ij}b_{ij}$ assumes small positive values at latter stages of simulation. Although instances of positive $\Phi^{(r)}_{ij}b_{ij}$ are observed, in the proximity of 2C limit (initial stages of evolution) $\Phi^{(r)}_{ij}b_{ij}$ is always negative. This implies that the pressure-strain correlation predominantly reduces the Reynolds stress anisotropy at this limit.

The RDT data demonstrate that the magnitude of $R1$ and $R2$ initially never

exceeds unity. Some results are shown in Fig. 3.2. In few cases, for example in AE (2C2) flow (Fig. 3.2b), $R1$ exceeds unity at long times. The conclusion then is that the magnitude of the redistribution does not, in general, exceed that of the production.

For strain-dominated mean flows, RDT results imply that the most likely behavior of the pressure-strain correlation is as follows (irrespective of the initial anisotropy):

- 1) $\Phi_{ij}^{(r)} = 0$, when $P''_{ij} = 0$;
- 2) $\Phi_{ij}^{(r)} b_{ij} \leq 0$ in the proximity of 2C turbulence.
- 3) $R1$ and $R2 \leq 1$.

In the rapid distortion limit, it would be reasonable to expect the models to display the same trends as RDT. We propose the first of the above characteristics of RDT as a rigorous mathematical constraint that a rapid pressure-strain correlation model must satisfy. We suggest the other two RDT characteristics as guidelines, the model violation of which should be minimized. Lacking dimensionality tensor information, one-point closures may not be able to capture the observed exceptions to criteria two and three. The model values of $\Phi_{ij}^{(r)} b_{ij}$, $R1$, and $R2$ must be scrutinized closely in the event of undesirable model behavior. Two categories of undesirable model behavior we investigate are: inconsistency with turbulence (RDT) physics and unrealizable evolution trajectories.

Inconsistency. If a turbulence model predicts evolution of Reynolds stress anisotropy when RDT indicates no evolution, the model is labeled as being inconsistent with turbulence physics. In Table 3.2, when a model shows evolution (denoted as ‘ER’ and ‘EU’), but the RDT does not (‘N’), we have inconsistency. For the first time, we pose consistency as a modeling constraint.

Unrealizability. As is common practice, a model is labeled as unrealizable, if it produces negative diagonal components of the Reynolds stress tensor (in the principal coordinates). In such a case, a model evolution trajectory passes from the realizable region (inside Lumley triangle) to the unrealizable area (outside Lumley triangle). The model evolution trajectories are tracked on the (ξ, η) invariant plane: where the invariants are defined by $6\eta^2 = b_{ij}b_{ji}$ and $6\xi^3 = b_{ij}b_{jk}b_{ki}$. To assess realizability violation, the outline of the Lumley invariant triangle is also shown. A trajectory is deemed unrealizable when it crosses the boundary of the Lumley triangle. In all cases identified with ‘EU’ (in Table 3.2), the model behavior is unrealizable.

3.4.2 Model calculations

Three models for the “rapid” part of the pressure-strain correlation (IP, LRR, and SSG) are now compared with the RDT data. The most fundamental aspects of the model calculations are tabulated in Table 3.2. In the table, ‘ER’ stands for an evolving realizable trajectory and ‘EU’ denotes an evolving unrealizable solution. The table demonstrates that in many cases models yield evolution of turbulence anisotropy when the RDT clearly shows no evolution. In other cases, when the RDT shows evolution, model behavior is unrealizable. We will now compare model calculations with RDT data and try to explain the physical failing underlying inconsistent and unrealizable model behavior. In particular, the connection between the violations and the proposed modeling guidelines will be sought.

Non-evolving cases

We discuss in detail, at first, the results from four cases: AC(1C2), AE(1C2), HS(1C1), and PS(1C1). The cases are identified by the mean flow and the initial

turbulence anisotropy (in parentheses). In these cases, RDT calculations show no evolution, as is seen from Table 3.2. Thus, $b_{ij}(t)=b_{ij}(0)$, $P''_{ij}b_{ij}=0$ and $\Phi^{(r)}_{ij}b_{ij}=0$. Models, however, demonstrate various behavior patterns including inconsistent and unrealizable evolution.

Case AC (IC2). All models predict spurious evolution in this case, but evolution trajectories stay inside the Lumley triangle (Fig. 3.4a). Thus, all three models considered predict inconsistent, but realizable behavior. To understand the origin of poor model behavior, we now examine the ratio $R1$ (Fig. 3.4b) and the invariants $P''_{ij}b_{ij}$ and $\Phi^{(r)}_{ij}b_{ij}$ (Fig. 3.4c). The initial value of $\Phi^{(r)}_{ij}\Phi^{(r)}_{ij}$ implied by each model is non-zero, while the $P''_{ij}P''_{ij}$ value is equal to zero as can be seen from $R1 \rightarrow \infty$ at $t = 0$ (Fig. 3.4b). Non-zero model $\Phi^{(r)}_{ij}$, then, causes the model trajectory to evolve. In RDT calculations, both $\Phi^{(r)}_{ij}$ and P''_{ij} are equal to zero resulting in no evolution. From Fig. 3.4(c), it is seen, that for each model, $P''_{ij}b_{ij}$ is positive and $\Phi^{(r)}_{ij}b_{ij}$ is negative. To summarize, all models violate criteria 1 and 3, and not criterion 2 in this case.

Case HS (IC1). The IP model predicts no anisotropy evolution in agreement with the RDT. In both cases - IP-model and RDT calculations - initial values of $\Phi^{(r)}_{ij}$ and P''_{ij} are equal to zero. Results from LRR and SSG models are shown in Fig. 3.5. The LRR model shows inconsistent and unrealizable behavior. The SSG model predictions are inconsistent, but realizable (Fig. 3.5a). From Fig. 3.5(b) it is clear that both models violate criteria 1 and 3. As regards criterion 2, the SSG model does not (Fig. 3.5c).

Case PS (IC1). In this case all models exhibit inconsistent and unrealizable behavior (Fig. 3.6a). All three models violate all three criteria (Figs. 3.6b and c).

Case AE (IC2). Again, all models predict inconsistent and unrealizable behavior (Fig.3.7a), and all three criteria are violated (Figs. 3.7b and c). The SSG model further

predicts that production tends to reduce anisotropy ($P''_{ij}b_{ij} < 0$), which is completely inconsistent with the RDT and turbulence physics.

Evolving cases

Now we consider cases where the RDT shows evolution of initial turbulence anisotropy (see Table 3.2). In all these cases, all three models show anisotropy evolution also. In this sense their behavior is consistent with the RDT. When a model predicts consistent and realizable behavior, no criterion violation is observed. Some examples are shown in Figs. 3.3 (a-c) for criterion 2 and in Figs. 3.2(a) and (b) for criterion 3. Results for all cases studied are summarized in Table 3.3. In many cases, the model evolution is unrealizable. As examples, cases AC (2C2) and PS (2C2) will be discussed in detail. *Case AC (2C2)*. The RDT trajectory starts from the 2C-axisymmetric turbulence corner of the Lumley triangle and evolves towards the 1C turbulence corner (Fig. 3.8a). All three model trajectories initially exit the Lumley triangle, but later recover and re-enter the realizability zone (Fig. 3.8a). The model prediction after the first trajectory exit from the Lumley triangle is irrelevant and, therefore, the model behavior must be deemed unrealizable. The reason for the violation can be seen in Fig. 3.3(d). The value of $\Phi^{(r)}_{ij}b_{ij}$ predicted by each model is initially positive leading to an increase of anisotropy level. At later times, the $\Phi^{(r)}_{ij}b_{ij}$ values become negative as the Reynolds stresses recover to realizable values. The RDT value of $\Phi^{(r)}_{ij}b_{ij}$ is always negative. Criterion 2 is violated, but not criterion 3 (Fig. 3.2c).

Case PS (2C2). The RDT trajectory is similar to the AC(2C2) case (Fig. 3.8b). All models are again unrealizable (Fig. 3.8b). The degree of violation in this case is much larger and there is no recovery to realizable values. The explanation is again found by investigating the behavior of $\Phi^{(r)}_{ij}b_{ij}$ presented in (Fig. 3.3e). The model values of

$\Phi^{(r)}_{ij}b_{ij}$ are positive and substantially larger than in the previous case making recovery to realizable values difficult. The RDT values are, again, always negative. Criterion 3 is not violated (Fig. 3.2d).

All the calculated results are summarized in Table 3.3. In the table, ‘C1’, ‘C2’, and ‘C3’ represent three criteria. Violation of a criterion is denoted by ‘V’ and non-violation is shown by ‘N’. Two other columns recording consistency and realizability are added in Table 3.3 to clearly demonstrate the connection between undesirable behavior and criteria violation. In these two columns, again ‘V’ indicates violation of consistency/realizability and ‘N’ shows non-violation. The connection between undesirable model behavior and modeling guideline violation is evident. Violations of criteria 1 and 3 are associated with spurious evolution and inconsistent model behavior. Violations of criterion 2 and realizability condition are correlated.

Implications of the RDT and model calculations are now summarized.

- 1) Without exceptions, the RDT data indicates that $\Phi^{(r)}_{ij}=0$, when $P''_{ij}=0$. Inconsistent model behavior is imminent when $\Phi^{(r)}_{ij}$ is non-zero as P''_{ij} vanishes. Therefore, criterion 1 is a mathematical constraint that a model must be mandated to satisfy. Another important inference is that for this combination of Reynolds stresses and mean velocity gradients, the “rapid” pressure-strain correlation assumes an unique value, which is zero.
- 2) From the results in this section, it is clear that $\Phi^{(r)}_{ij}b_{ij}$ being positive (in the proximity of 2C turbulence) is not a desirable feature in a model, since all observed realizability violations are associated with such behavior. In all these cases, the RDT values of $\Phi^{(r)}_{ij}b_{ij}$ are negative in 2C limit. The underlying physics is now explained. When $\Phi^{(r)}_{ij}b_{ij}$ is positive, the model extracts energy from low-energy components and deposits it into high-energy components. This action continues even when the low-energy component is completely depleted, driving that component into negative values.

Mathematically, this is much like counter-gradient transport, which almost always has a destabilizing influence. While the RDT data does permit this destabilizing energy transfer in some instances, physics incumbent in the RDT equations ensures a delicate balance between production and redistributive processes leading to realizable behavior. It remains to be seen if single-point closure models can be developed to replicate this delicate balance. Until this issue is addressed satisfactorily, criterion 2 must be considered as an important constraint that a one-point closure model should satisfy in the proximity of 2C turbulence to avoid the risk of unrealizable behavior. Motivated by these findings, Sambasivam³⁰ investigated the realizability violations in turbulence calculations using various linear and non-linear rapid pressure-strain models. Complete model calculations (including slow pressure-strain correlation and dissipation terms) starting from initial conditions spanning the entire Lumley triangle, were performed for different types of homogenous turbulence. It was found that every single episode of realizability violation was accompanied by $\Phi^{(r)}_{ij}b_{ij}$ being positive. While not all instances of $\Phi^{(r)}_{ij}b_{ij}$ in the interior led to unrealizable trajectories, every unrealizable trajectory did exhibit positive $\Phi^{(r)}_{ij}b_{ij}$. Every trajectory that exhibited $\Phi^{(r)}_{ij}b_{ij}$ at the 2C turbulence limit, did become unrealizable. To a large extent, this finding validates the importance of the proposed modeling guideline.

Much like criterion 2, criterion 3 appears to be physically reasonable in the proximity of 2C turbulence. This criterion also suggests approximate bounds on the pressure-strain correlation magnitude: $0 \leq \Phi^{(r)}_{ij}\Phi^{(r)}_{ij} \leq P''_{ij}P''_{ij}$. Thus, the larger the anisotropy production, the wider is the range of values that the correlation can take. The margin of error incurred in pressure-strain correlation modeling is therefore likely to increase with increasing anisotropy production, even with the most accurate models.

3.5 CONCLUSION

In the rapid distortion limit, turbulence evolution depends on various factors: type of anisotropy, degree of anisotropy, velocity spectrum tensor, and the imposed mean-flow deformation. Consequently, the pressure-strain correlation term will also depend on these parameters, especially the so-called dimensionality tensor. While the behavior of the pressure-strain correlation can be quite complex and not easily generalized in anisotropic turbulence, certain physical features can be identified as being common for a

variety of dimensionality tensors. The RDT calculations performed in this research show that in mean strain-dominated flows the dynamics of turbulence is such that:

- 1) $\Phi_{ij}^{(r)} = 0$, when $P''_{ij} = 0$.
- 2) $\Phi_{ij}^{(r)} b_{ij} \leq 0$ in the proximity of 2C turbulence.
- 3) $0 \leq \Phi_{ij}^{(r)} \Phi_{ij}^{(r)} \leq P''_{ij} P''_{ij}$ in the proximity of 2C turbulence.

It is proposed that criterion 1 be used as a rigorous mathematical constraint and the other two as guidelines for developing “rapid” pressure-strain correlation models.

Reynolds stress transport model calculations performed at the rapid distortion limit display unphysical (inconsistent) and unrealizable behavior for some initial turbulence anisotropies and mean flows. Inconsistent behavior refers to spurious evolution predicted by a model when the RDT indicates no change in anisotropy from its initial level. Clearly, in a full-turbulence equation set, there may be evolution from an anisotropic initial state, but this evolution must be initiated by “slow” pressure-strain correlation or dissipation terms.

Close examination of the RSTM results reveal that both unrealizable and inconsistent model behavior can be directly related in the investigated cases to violations

of the guidelines proposed. Inconsistent behavior occurs when the model pressure-strain correlation does not vanish as the production of anisotropy goes to zero. Unrealizable model behavior is observed when the model pressure-strain correlation unphysically attempts to increase anisotropy rather than diminish it at the 2C turbulence state.

The results and analysis presented in this research should aid in better understanding the role of the pressure-strain correlation in turbulence and hence, enable us to develop improved models for this term. Similar examination of mean rotation-dominated flows will be undertaken in the future.

Table 3.1 Model coefficients for expression (3.12)

	LRR-IP	LRR-QI	SSG
C_1^1	0	0	1.8
C_2^0	0.8	0.8	0.8
C_2^1	0	0	1.3
C_3	1.2	1.75	1.25
C_4	1.2	1.31	0.4

Table 3.2 Summary of RDT and IP, LRR, SSG model calculation results. Notations: (E) evolving trajectory; (N) no evolving; (U) unrealizable evolution; (R) realizable evolution. 1C3 (AC, AE) case is equivalent to 1C2 (AC, AE); and 2C3 (AC, AE) case is equivalent to 2C2 (AC, AE).

Initial conditions	Flow	Solution trajectories			
		RDT	Model		
			IP	LRR	SSG
1C1	AC	N	EU	EU	EU
	AE	N	ER	ER	ER
	PS	N	EU	EU	EU
	HS	N	N	EU	ER
1C2	AC	N	ER	ER	ER
	AE	N	EU	EU	EU
	PS	N	ER	ER	ER
	HS	E	ER	ER	ER
1C3	PS	N	N	EU	EU
	HS	N	N	EU	EU
2C1	AC	N	ER	ER	ER
	AE	N	EU	EU	EU
	PS	E	ER	ER	ER
	HS	E	ER	ER	ER
2C2	AC	E	EU	EU	EU
	AE	E	ER	ER	ER
	PS	E	EU	EU	EU
	HS	N	N	ER	ER
2C3	PS	E	ER	ER	ER
	HS	E	ER	ER	ER
isotropic	AC	E	ER	ER	ER
	AE	E	ER	ER	ER
	PS	E	ER	ER	ER
	HS	E	ER	ER	ER

Table 3.3 IP, LRR, SSG model behavior assessment in RD limit. Notations: (C1) criterion 1; (C2) criterion 2; (C2) criterion 3 (C3); (N) non-violation; (V) violation.

Mean flow	Anisotropy condition	Model	Realizability	Consistency	C1	C2	C3	
AC	1C1	IP	V	V	V	V	V	
		LRR	V	V	V	V	V	
		SSG	V	V	V	V	V	
	1C2	IP	N	V	V	N	V	
		LRR	N	V	V	N	V	
		SSG	N	V	V	N	V	
	2C1	IP	N	V	V	N	V	
		LRR	N	V	V	N	V	
		SSG	N	V	V	N	V	
	2C2	IP	V	N	N	V	N	
		LRR	V	N	N	V	N	
		SSG	V	N	N	V	N	
AE	1C1	IP	N	V	V	N	V	
		LRR	N	V	V	N	V	
		SSG	N	V	V	N	V	
	1C2	IP	V	V	V	V	V	
		LRR	V	V	V	V	V	
		SSG	V	V	V	V	V	
	2C1	IP	V	V	V	V	V	
		LRR	V	V	V	V	V	
		SSG	V	V	V	V	V	
	PS	1C1	IP	V	V	V	V	V
			LRR	V	V	V	V	V
			SSG	V	V	V	V	V
1C2		IP	N	V	V	N	V	
		LRR	N	V	V	N	V	
		SSG	N	V	V	N	V	
1C3		LRR	V	V	V	V	V	
		SSG	V	V	V	V	V	
2C2		IP	V	N	N	V	N	
		LRR	V	N	N	V	N	
		SSG	V	N	N	V	N	
HS		1C1	LRR	V	V	V	V	V
	SSG		N	V	V	N	V	
	1C3	LRR	V	V	V	V	V	
		SSG	V	V	V	V	V	
	2C2	LRR	N	V	V	N	V	
		SSG	N	V	V	N	V	

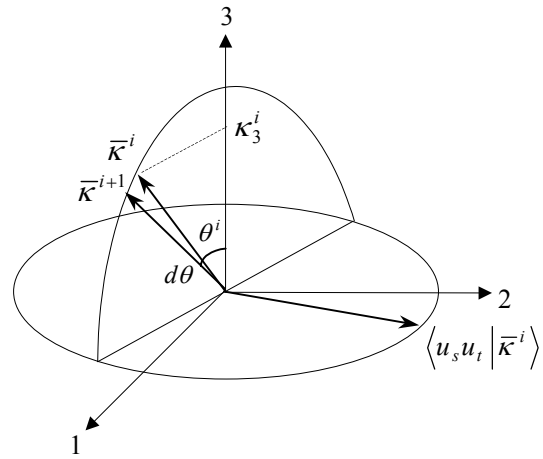


Figure 3.1 Coordinate scheme for the 2C3 initial turbulence state.

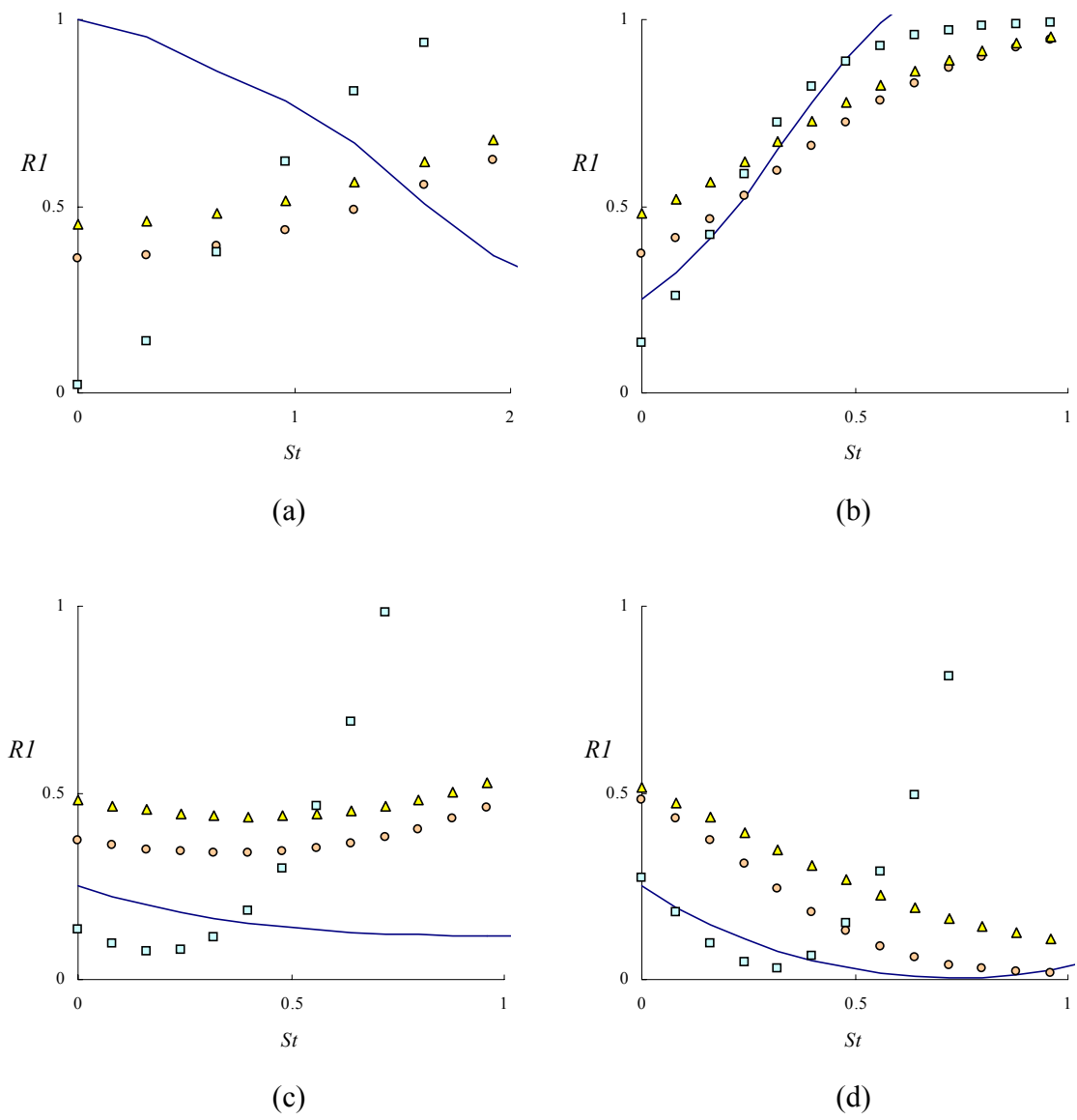


Figure 3.2 Evolution of the ratio $R1$ for various cases, a) HS (1C2), b) AE (2C2), c) AC (2C2), d) PS (2C2). **Notations :** (—) RDT, (○) IP, (△) LRR, (□) SSG.

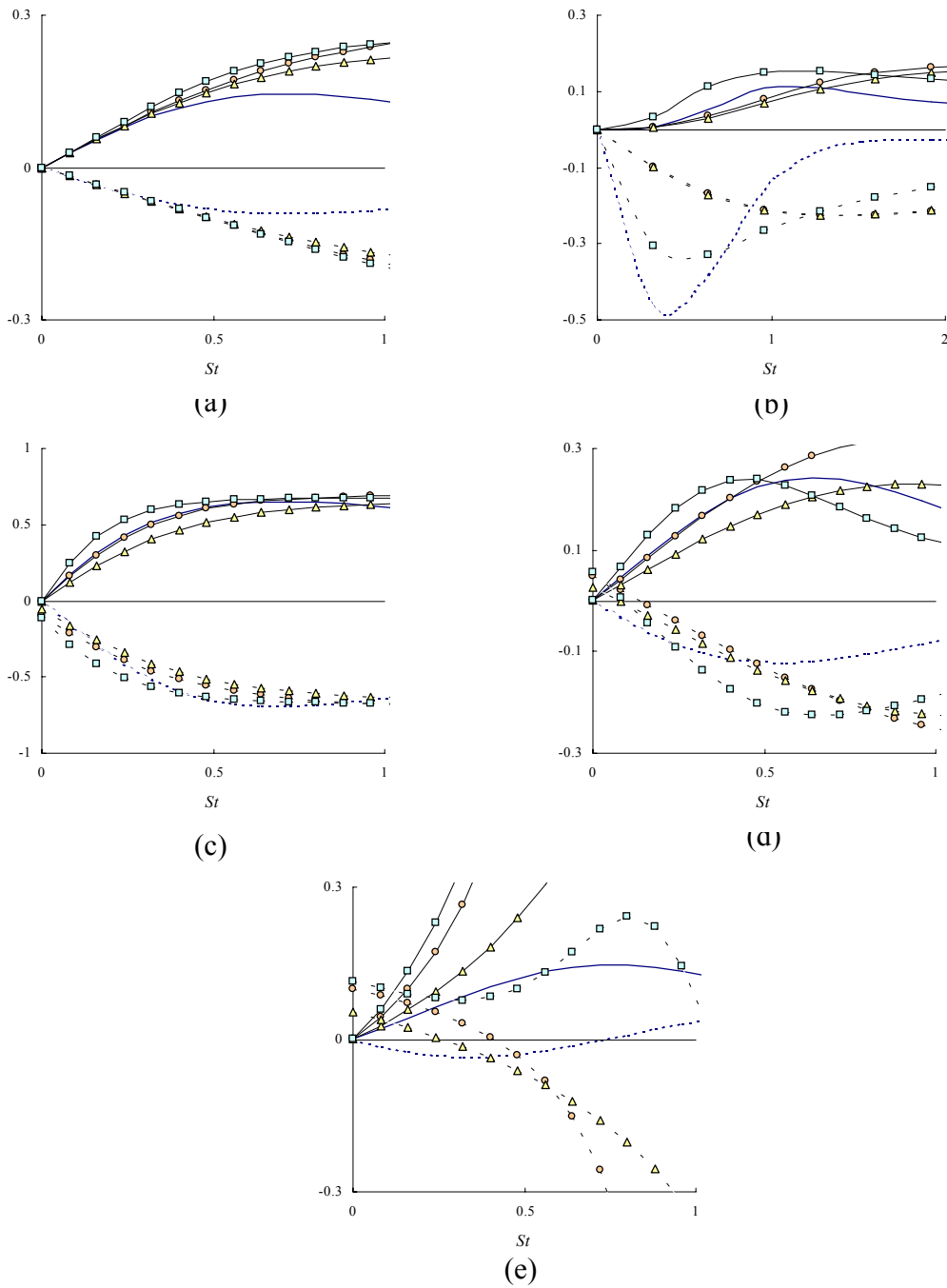


Figure 3.3 Evolution of P''_{ijbij} and $\Phi^{(r)}_{ijbij}$, a) PS (isotropic), b) HS (1C2), c) AE (2C2), d) AC (2C2), e) PS (2C2). **Notations:** for P''_{ijbij} , (—) RDT, (○—) IP, (△—) LRR, (□—) SSG; for $\Phi^{(r)}_{ijbij}$, (- -) RDT, (○--) IP, (△--) LRR, (□--) SSG.

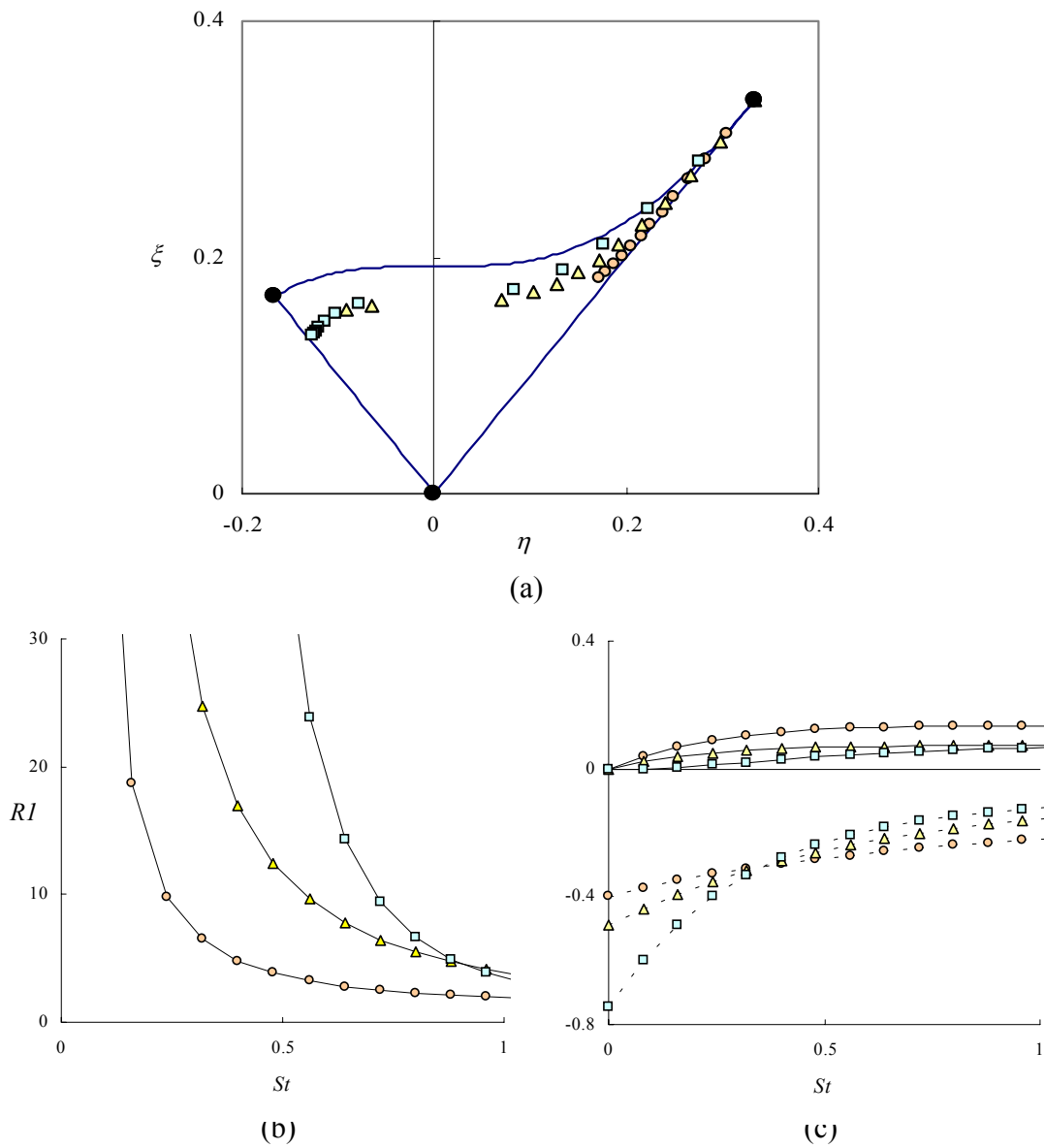


Figure 3.4 AC flow with 1C2 initial turbulence state: a) Lumley triangle, b) evolution of the $R1$ parameter, c) evolution of invariants $P''_{ij}b_{ij}$ and $\Phi^{(r)}_{ij}b_{ij}$. The black dots (\bullet) denote the corners of Lumley triangle corresponding to isotropic, 2C, and 1C conditions. Other notations are the same as in Figs. 3.2 and 3.3.

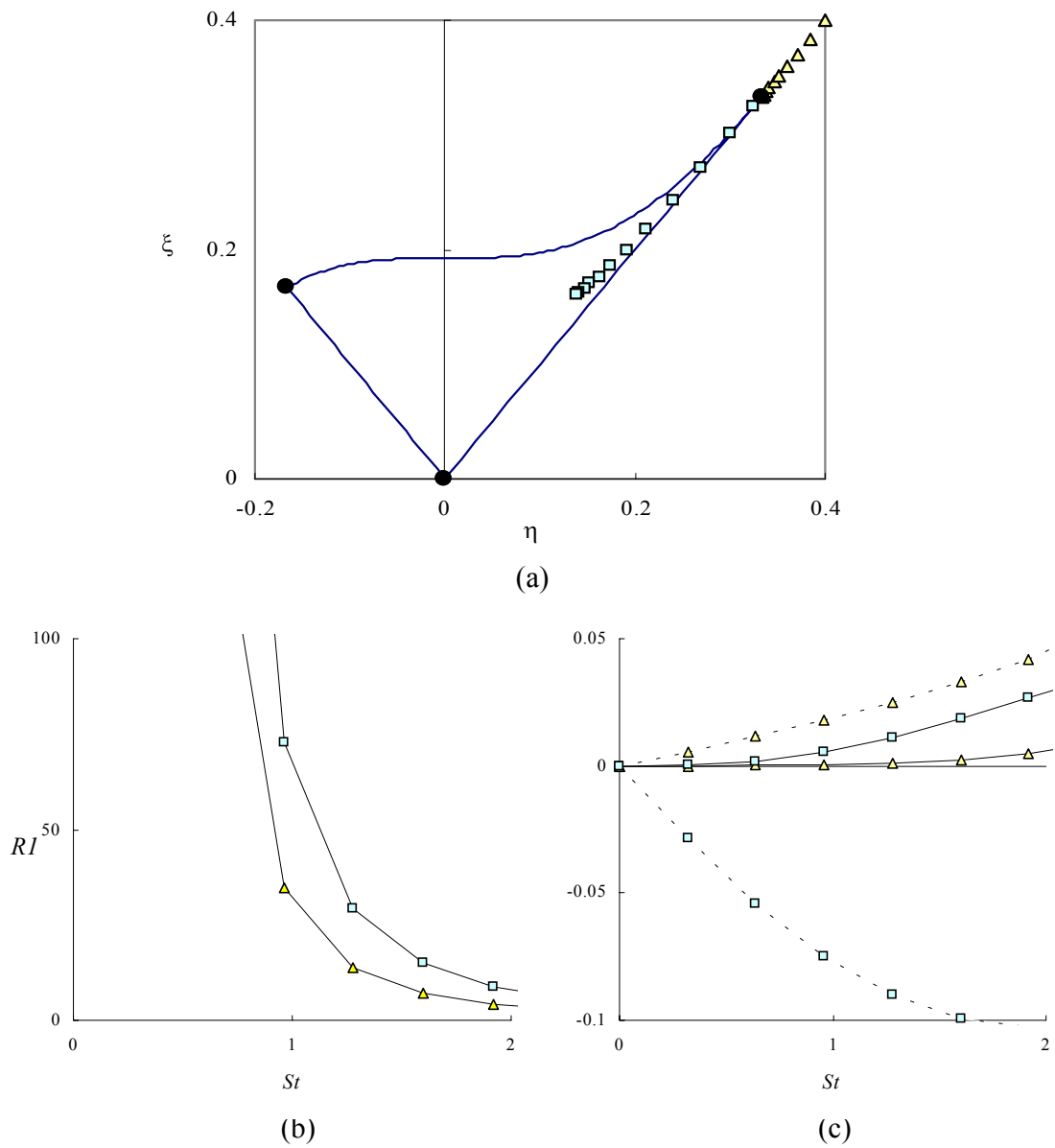


Figure 3.5 HS flow with 1C1 initial turbulence state: a) Lumley triangle, b) evolution of the $R1$ parameter, c) evolution of invariants $P''_{ij}b_{ij}$ and $\Phi^{(1)}_{ij}b_{ij}$. Notations are the same as in Figs. 3.4.

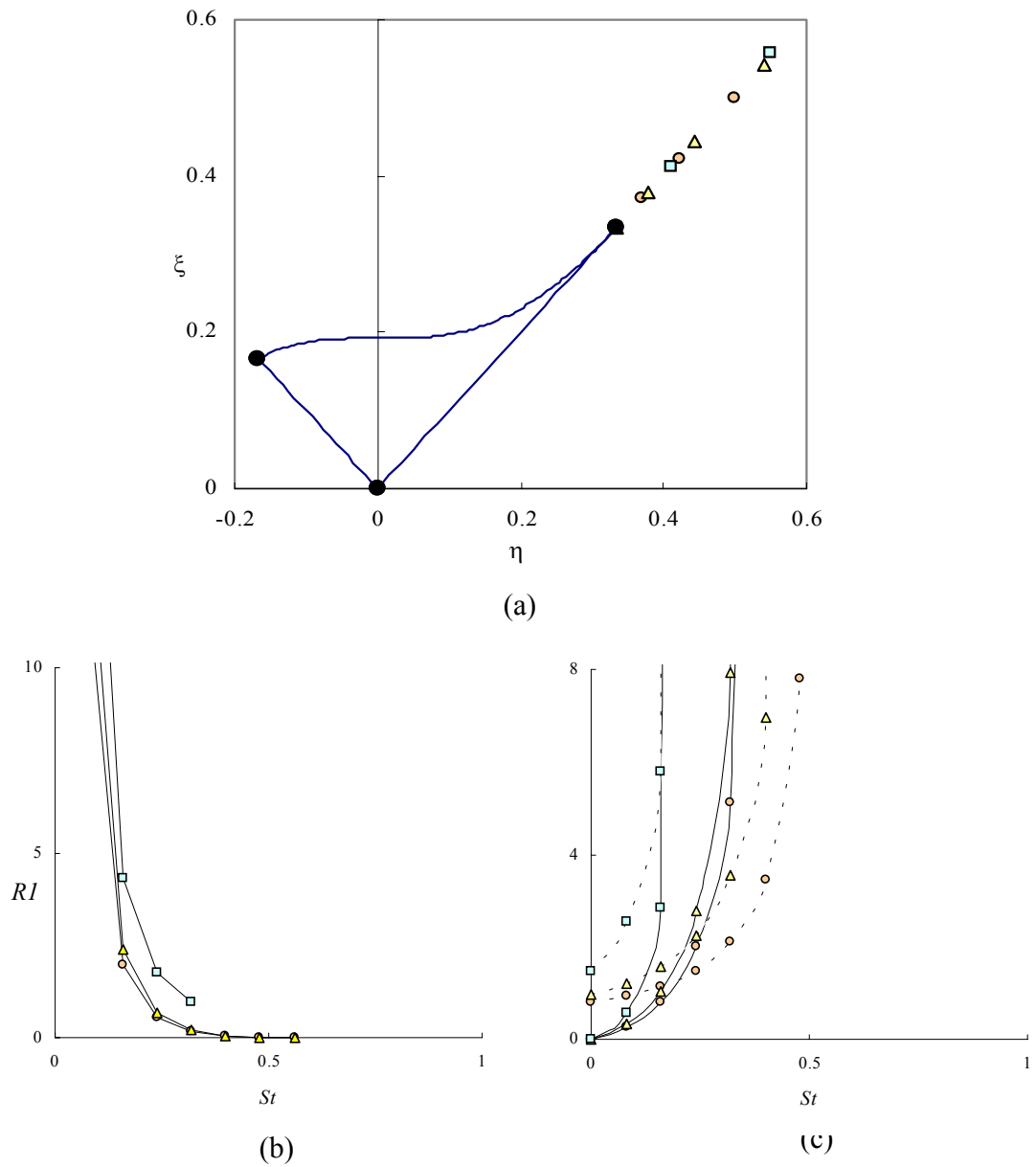


Figure 3.6 PS flow with 1C1 initial turbulence state: a) Lumley triangle, b) evolution of the $R1$ parameter, c) evolution of invariants $P''_{ij}b_{ij}$ and $\Phi^{(r)}_{ij}b_{ij}$. Notations are the same as in Figs. 3.4.

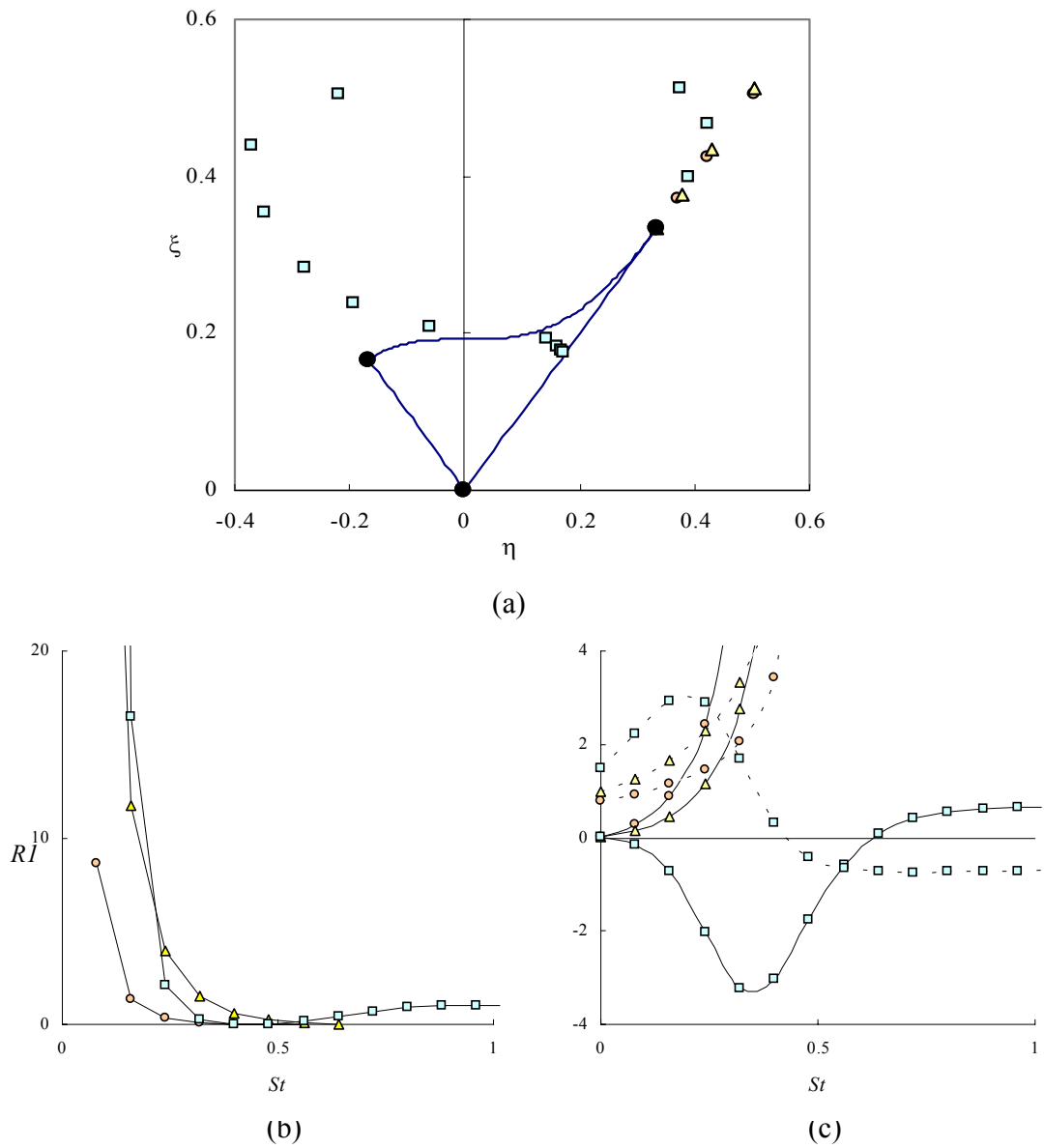


Figure 3.7 AE flow with 1C2 initial turbulence state: a) Lumley triangle, b) evolution of the $R1$ parameter, c) evolution of invariants $P''_{ij} b_{ij}$ and $\Phi^{(r)}_{ij} b_{ij}$. Notations are the same as in Figs. 3.4.

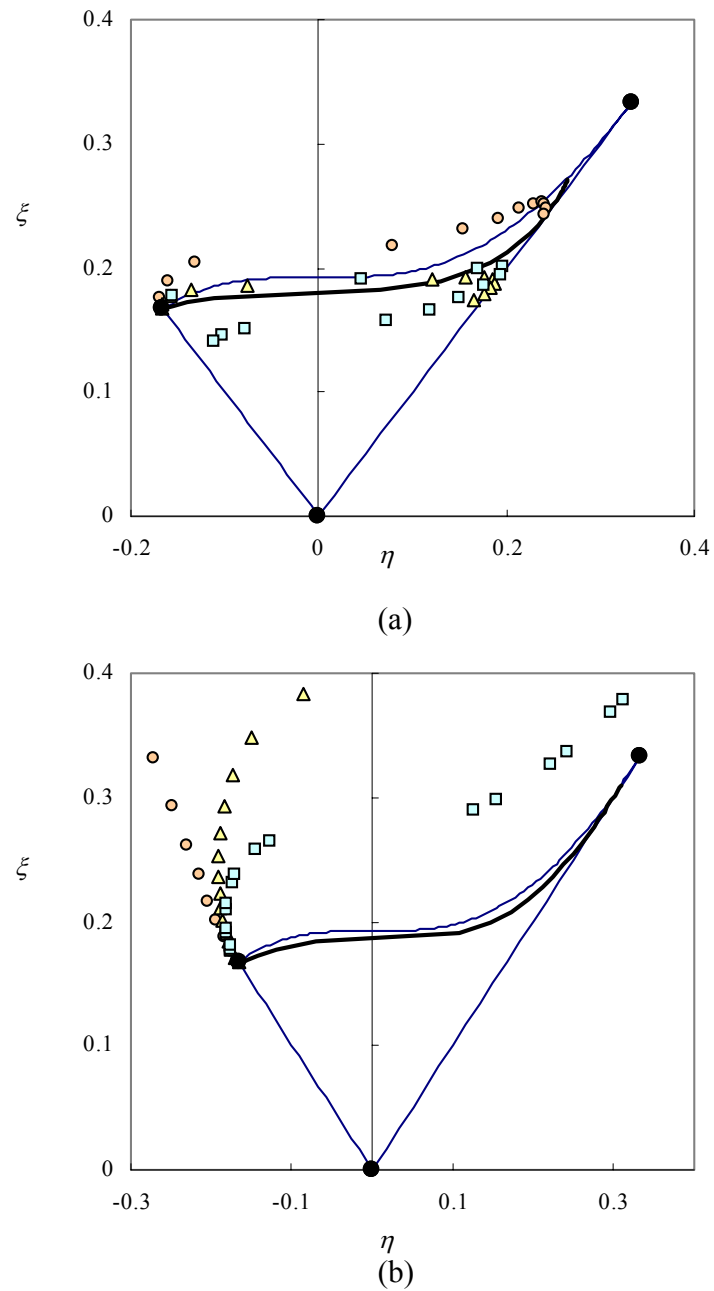


Figure 3.8 Solution trajectories in the Lumley triangle, a) AC (2C2 and isotropic), b) PS (2C2 and isotropic). **Notations** : (—) RDT, (○) IP model, (△) LRR model, (□) SSG model for initially anisotropic turbulence. The corners of Lumley triangle are marked with (●).

CHAPTER IV

UNSTEADY COMPUTATION OF TURBULENT FLOW PAST A SQUARE CYLINDER USING PARTIALLY-AVERAGED NAVIER-STOKES (PANS) METHOD

In this chapter, the final topic, “unsteady computation of turbulent flow past a square cylinder using Partially-Averaged Navier-Stokes (PANS) method” is covered. The PANS method – a bridging model between Reynolds Averaged Navier-Stokes (RANS) method and Large eddy Simulation (LES) – is used to calculate the flow past a square cylinder. PANS calculations are performed at various levels of physical resolution, and the solutions are compared with experimental data and LES computation. The result shows that more and more flow features are captured as the physical resolution improves with decreasing f_k (PANS resolution control parameter). Overall, all results compared – Strouhal number (S_t), mean/RMS drag coefficient (C_D), RMS lift coefficient (C_L) and mean/fluctuating velocity field data at various locations – monotonically go from RANS to the experimental results with increasing scale resolution. PANS method appears capable of capturing many important unsteady flow features at an affordable computational effort.

4.1 INTRODUCTION

Flow past a bluff body is of practical importance in many engineering applications. In this flow, boundary layer, shear layer, and wake flow exist at the same time and interact with each other to generate very complicated flow features such as

separation, reattachment, recirculation, unsteady vortex shedding, three-dimensional flow features, and so on. Vortex shedding induces a pulsating pressure field that leads to time-dependant loading on bluff body and generation of acoustic noise over the entire flow field. Clear understanding of these phenomena is important for addressing structural and environmental issues.

The flow past a square cylinder is an idealized bluff-body problem that has been subject to a great deal of experimental and computational investigations. Accurate calculation of this unsteady turbulent flow requires resolving large unsteady scales of motion to some extent. The traditional Reynolds averaged Navier-Stokes (RANS) type statistical models are not suitable for this application because not only small-scale turbulent motions but also the geometry-dependant large eddy motions are modeled. Large Eddy Simulation (LES) and Direct Numerical Simulation (DNS) are physically appropriate tools for the calculation of unsteady turbulent flows. Recently, the flow past a square cylinder has served as a benchmark for testing various sub-grid scale models^{31,32,33}. However, because of the overwhelming requirement of computing power, LES and DNS are still not practical tools for engineering applications. As a compromise, several strategies for combining the best feature of RANS method and LES are being developed³⁴⁻³⁷.

Recently, Girimaji³⁸ proposed partially-averaged Navier-Stokes (PANS) method – a bridging model between RANS method and LES – which is based on the averaging-invariant property³⁹ of the Navier-Stokes equation. In this research, we solve the flow past a square cylinder problem using PANS method and perform a detailed comparison with existing experimental and LES data.

As widely accepted, the RANS models are the most sophisticated one-point closures. In these closures, complicated physics such as curvature and

rotation can be accurately modeled and different physical processes like return to isotropy, dissipation, and production can be accounted for appropriately. Furthermore, important issues such as realizability and consistency with various limiting cases of physics can be incorporated accurately. According to Girimaji³⁸, the failure of the classical RANS method in solving unsteady turbulent flow (so-called URANS approach) is due to its incorrect adaptation rather than inherent model deficiency. The PANS method rectifies the incorrect adaptation in RANS for resolving large unsteady fluctuations by introducing partial averaging concept. The extent of partial averaging is determined implicitly by pre-specified fraction of unresolved turbulent energy (f_k) and unresolved dissipation rate (f_ϵ). These two parameters actively control the physical resolution of the computation. The PANS model, subject to minor assumptions, is a formal cutoff wave-number sensitive adaptation of the existing RANS models.

The PANS method entails the computation of evolution equation for resolved field along with a two-equation closure model for the sub-filter stresses. The sub-filter stress is the generalized second order central moment³⁹ that is modeled using Bossinesq approximation. Evolution equations for sub-filter kinetic energy and dissipation rate are solved to complete the model closure.

The organization of this chapter is as follows: we will present the PANS model equations followed by the details of the computation of the flow past a square cylinder. The calculation results and discussion are presented next and a summary/conclusion will be given at the end.

4.2 PANS MODEL EQUATIONS

The incompressible Navier-Stokes equations is

$$\frac{\partial V_i}{\partial t} + V_j \frac{\partial V_i}{\partial x_j} = -\frac{\partial p}{\partial x_i} + \nu \frac{\partial^2 V_i}{\partial x_j \partial x_j}. \quad (4.1)$$

Consider a general filtering operation that is linear and constant preserving³⁹. The instantaneous velocity field is decomposed into resolved velocity field (U_i) and unresolved velocity field (u_i):

$$V_i = U_i + u_i, \text{ where } U_i = \langle V_i \rangle. \quad (4.2)$$

The angular bracket represents a general filtering (or averaging) operator that commutes with time and space differentiation. The resolved velocity field is loosely identified as the velocity associated with non-universal large-scale structure that is calculated fully and the unresolved velocity field is taken to be the background turbulent field. Each velocity field satisfies continuity condition such that

$$\frac{\partial U_i}{\partial x_i} = \frac{\partial u_i}{\partial x_i} = 0. \quad (4.3)$$

For this arbitrary filtering process, the average of unresolved velocity and the correlation between resolved and unresolved velocities are non-zero³⁹,

$$\langle u_i \rangle \neq 0, \quad \langle U_i u_j \rangle \neq 0. \quad (4.4)$$

We consider the generalized central moments³⁹ $\tau(f, g)$ and $\tau(f, g, h)$ defined by

$$\tau(f, g) = \langle fg \rangle - \langle f \rangle \langle g \rangle, \quad (4.5)$$

$$\tau(f, g, h) = \langle fgh \rangle - \langle f \rangle \tau(g, h) - \langle g \rangle \tau(f, h) - \langle h \rangle \tau(f, g) - \langle f \rangle \langle g \rangle \langle h \rangle. \quad (4.6)$$

Then, from the equations (4.1) to (4.6), the evolution equations of the resolved velocity and the generalized second moment (sub-filer stress) can be written as

$$\frac{\partial U_i}{\partial t} + U_j \frac{\partial U_i}{\partial x_j} = -\frac{\partial p_U}{\partial x_i} + \nu \frac{\partial^2 U_i}{\partial x_j \partial x_j} - \frac{\partial \tau(V_i, V_j)}{\partial x_j}, \quad (4.7)$$

$$\begin{aligned}
& \frac{\partial \tau(V_i, V_j)}{\partial t} + U_k \frac{\partial \tau(V_i, V_j)}{\partial x_k} \\
&= -\frac{\partial}{\partial x_k} \left(\tau(V_i, V_j, V_k) + \tau(p, V_i) \delta_{jk} + \tau(p, V_j) \delta_{ik} - \nu \frac{\partial \tau(V_i, V_j)}{\partial x_k} \right), \quad (4.8) \\
& \quad - \tau(V_i, V_k) \frac{\partial U_j}{\partial x_k} - \tau(V_j, V_k) \frac{\partial U_i}{\partial x_k} + 2\tau(p, s_{ij}) - 2\nu \tau \left(\frac{\partial V_i}{\partial x_k}, \frac{\partial V_j}{\partial x_k} \right)
\end{aligned}$$

$$p_U = \langle p \rangle; \quad s_{ij} = \frac{1}{2} \left(\frac{\partial U_i}{\partial x_j} + \frac{\partial U_j}{\partial x_i} \right). \quad (4.9)$$

The evolution equation for the unresolved turbulent kinetic energy,

$$K_u = \frac{1}{2} \tau(V_i, V_i), \quad (4.10)$$

comes directly from the contraction of equation (4.8) :

$$\frac{\partial K_u}{\partial t} + U_k \frac{\partial K_u}{\partial x_k} = -\frac{\partial}{\partial x_k} \left(\tau(V_i, V_i, V_k) + \tau(p, V_k) - \nu \frac{\partial K_u}{\partial x_k} \right) + P_u - \varepsilon_u. \quad (4.11)$$

P_u and ε_u are the production and dissipation rate of unresolved turbulent kinetic energy :

$$P_u = -\tau(V_i, V_k) \frac{\partial U_i}{\partial x_k}; \quad \varepsilon_u = \nu \tau \left(\frac{\partial V_i}{\partial x_k}, \frac{\partial V_i}{\partial x_k} \right). \quad (4.12)$$

As pointed out by Germano³⁹, the evolution equations of the generalized central moments of any order are invariant to the type of filter operation. If the averaging range is expanded to integral length scale (represented by over-bar), equation (4.7) and (4.8) become RANS equation ($\langle V_i \rangle = U_i = \bar{V}_i$). By replacing the averaging process with a typical filter operator ($\langle V_i \rangle = U_i = L(V_i)$, L is the filter operator), equation (4.7) and (4.8) become the governing equations for LES.

In PANS method, there is no such an explicit relationship between resolved and instantaneous velocity because the averaging is implicit in nature. The extent of the partial averaging – equivalently, the physical resolution – in PANS is determined by two

control parameters: the ratio of the unresolved kinetic energy to the total fluctuating kinetic energy ($f_k = K_u/K$) and the ratio of the unresolved dissipation rate to the total fluctuating dissipation rate ($f_\varepsilon = \varepsilon_u/\varepsilon$). The total fluctuating kinetic energy (K) and the total fluctuating dissipation rate (ε) are defined as

$$K = \frac{1}{2} \overline{(V_i - \bar{V}_i)(V_i - \bar{V}_i)}; \quad \varepsilon = \nu \frac{\partial \overline{(V_i - \bar{V}_i)}}{\partial x_j} \frac{\partial \overline{(V_i - \bar{V}_i)}}{\partial x_j}. \quad (4.13)$$

Rather than a pre-determined cutoff as in LES, the PANS cutoff wave-number varies according to the pre-specified f_k value. By suitably choosing f_k and f_ε , implied cut-off can be placed any part of energy spectrum including dissipation range.

The roles of f_k and f_ε can be understood in following way. When the Reynolds number is high enough, most of the dissipation occurs in the smallest scales of motion. If the implied cutoff is in the inertial range, it is reasonable to expect that f_ε is unity. This means all of dissipation rate is modeled. The different settings of the f_k value actively control the resolution of the flow motion. Setting f_k equal to unity means all fluctuating motion is modeled. In this case, PANS reverts back to standard K - ε model. The smaller the f_k value, the larger the number of scales of motions captured by solving the resolved velocity field. The appropriate value for f_k will depend on physical resolution requirement and the flow field on consideration. The limiting case of $f_k = f_\varepsilon = 0$ corresponds to DNS.

To solve the resolved field equation, a constitutive relation between unresolved field stress and the resolved flow field is needed. It is reasonable to argue that the background turbulence is 'universal' enough to be represented by one-point turbulence closure. We will adopt the Bossinesq approximation in the PANS closures :

$$\tau(V_i, V_j) = -\nu_u \left(\frac{\partial U_i}{\partial x_j} + \frac{\partial U_j}{\partial x_i} \right) + \frac{2}{3} K_u \delta_{ij} \quad \text{where } \nu_u = C_\mu \frac{K_u^2}{\varepsilon_u}. \quad (4.14)$$

Starting from the standard K - ε equations and invoking the averaging-invariance property, Girimaji³⁸ derived the evolution equation for K_u and ε_u :

$$\begin{aligned} \frac{dK_u}{dt} &= \frac{\partial K_u}{\partial t} + U_j \frac{\partial K_u}{\partial x_j} = P_u - \varepsilon_u + \frac{\partial}{\partial x_j} \left(\frac{v_u}{\sigma_{ku}} \frac{\partial K_u}{\partial x_j} \right); \\ \frac{d\varepsilon_u}{dt} &= \frac{\partial \varepsilon_u}{\partial t} + U_j \frac{\partial \varepsilon_u}{\partial x_j} = C_{\varepsilon 1}^* \frac{P_u \varepsilon_u}{K_u} - C_{\varepsilon 2}^* \frac{\varepsilon_u^2}{K_u} + \frac{\partial}{\partial x_j} \left(\frac{v_u}{\sigma_{\varepsilon u}} \frac{\partial \varepsilon_u}{\partial x_j} \right); \\ \sigma_{ku} &= \frac{f_k^2 \sigma_k}{f_\varepsilon}; \quad \sigma_{\varepsilon u} = \frac{f_k^2 \sigma_\varepsilon}{f_\varepsilon}; \quad C_{\varepsilon 1}^* = C_{\varepsilon 1}; \quad C_{\varepsilon 2}^* = \frac{f_k}{f_\varepsilon} (C_{\varepsilon 2} - C_{\varepsilon 1}) + C_{\varepsilon 1}. \end{aligned} \quad (4.15)$$

The constants σ_k , σ_ε , $C_{\varepsilon 1}$, and $C_{\varepsilon 2}$ are those of the standard K - ε model.

The basic PANS model rationale can be understood by comparing the eddy viscosity of the unresolved scales (ν_u) and that of total fluctuations or RANS ($\nu_T = C_\mu K^2 / \varepsilon$). If the implied cut-off wave-number is in the range that is smaller than that of energy-containing scale or in the inertial range, then

$$\frac{\nu_u}{\nu_t} = \frac{C_\mu K_u^2 / \varepsilon_u}{C_\mu K^2 / \varepsilon} \approx \left(\frac{K_u}{K} \right)^2 \ll 1. \quad (4.16)$$

If the PANS model can produce unresolved kinetic energy and unresolved dissipation rate satisfying the conditions

$$K_u < K \quad \text{and} \quad \varepsilon_u = \varepsilon, \quad (4.17)$$

the eddy viscosity value of the PANS will be much smaller than that of RANS and PANS model can resolve more scales of motion than RANS model.

In summary, equations (4.3), (4.7), (4.14), and (4.15) combine to form the PANS model. The model equations are basically in the same form as the standard K - ε model. The primary differences are in the model coefficients. This means that existing CFD codes with standard K - ε models can be easily converted into PANS code with

minor changes.

4.3 COMPUTATION

For comprehensive comparison with the existing data^{33,40-45}, the PANS model calculation is performed at $Re=U_oD/\nu=22,000$ (D : cylinder edge length). The f_ε value is set to unity in all calculations. To assess the capability of resolution control of the PANS model, various values of f_k ($=1.0, 0.7$ and 0.4) that cover the range of RANS to LES are chosen. The Cartesian coordinate system has been used in describing the flow field. The square cylinder is aligned in z (spanwise)-direction and inlet flow is set in x (streamwise)-direction. The computational domain and dimensions are shown in figure 4.1. A total 18 cells have been imposed along the cylinder edge. Uniform grid is used in span-wise direction. The simulation conditions and geometry are tabulated in table 4.1. In order to isolate the effect of the model from grid resolution, all the cases are computed on the same 3-dimensional grid. It must be pointed out that both $f_k=1.0$ and 0.7 case can be computed on much coarser grids. In fact, $f_k=1.0$ (RANS) case requires only a 2-dimensional grid. However, for smaller f_k values, more scales of motions are captured and a full 3-dimensional calculation is needed.

For the flow simulation, FLUENT – a commercial CFD program – has been used with appropriate change in model equation of unresolved kinetic energy and unresolved dissipation rate according to equation (4.15). Time marching has been performed with constant time step ($\Delta t=0.025$). Standard inflow and outflow boundary conditions are used at inlet and outlet. The log-law wall function is used at the wall boundary of cylinder. This means that f_k is set to unity at the wall adjacent cells for every case as is typical of detached eddy simulation (DES). The lateral (y -direction) boundaries are also subject to wall boundary condition to make the simulation

comparison with experimental data more accurate ($H=14D$ is the exactly the same value as Lyn's experiment⁴⁵). For the boundary condition of the unresolved turbulent quantities at inlet, turbulence intensity is set to 2%. The ratio of unresolved eddy viscosity to molecular viscosity is set to a typical value⁴⁸ of 10, from which inlet unresolved dissipation rate is calculated. Periodic boundary condition is imposed in the span-wise direction.

After each flow is fully developed, the data are gathered to calculate flow statistics. The instantaneous resolved quantity is decomposed into time-spanwise ensemble averaged quantity and fluctuating quantity (e.g., $U_i(t) = (U_i)_{mean} + u'$). All of the data plots are based on this decomposition.

4.4 RESULTS AND DISCUSSION

Apart from integrated flow parameters data – Strouhal number (S_t), drag coefficient (C_D), and lift coefficient (C_L) –, near wake mean and fluctuating velocity field data are also calculated and compared with experiment and LES. For the statistical data, about ten shedding cycles of instantaneous data are used for $f_k = 1.0$ and 0.7 cases. In these two cases, the flow field shows nearly regular shedding pattern and ten 10 shedding cycles are adequate for computing statistics. In case of $f_k = 0.4$, however, due to larger degree of fluctuations in all directions, more than 30 shedding cycles of data are used for compiling statistics.

Many experiments on flow past a square cylinder are focused on force exerted by the flow on the body⁴⁰⁻⁴³, rather than on the details of flow field itself. One of earliest detailed flow-field measurements can be found in Durao et. al.⁴⁴ for $Re=14,000$ and more complete measurements of $Re=21,400$ are given in Lyn et. al.⁴⁵. Above data are used for evaluating PANS calculation results. Of the many LES computations in

literature, the results of Sohankar et. al.³³ (Re=22,000) have been selected for the comparison with PANS. For the velocity field data the comparison, only Smagorinsky sub-grid scale model result in Sohankar has been used.

We first perform a grid and time-step convergence study in 2-dimensional domain (see the dotted line in figure 4.1). For this study, f_k is set to 0.7. A cut of 3-dimensional grid specified in table 4.1 is used as a reference grid. For time step convergence test, five different time steps ($\Delta t = 0.025, 0.05, 0.1, 0.25, \text{ and } 0.5$) are chosen and calculated in the reference grid. For grid size convergence test, four different grids are used with the same time step as in full 3-dimensional calculation ($\Delta t = 0.025$). Each grid is coarsened or fined in constant ratio that is parameterized as the number of grid cells divided by the number of reference grid cells. The selected ratios are 1.5, 1.0, 0.55, and 0.25. Unresolved turbulent kinetic energy and dissipation rate are volume averaged over entire 2-dimensional domain and their behaviors are plotted in figure 4.2. As can be seen in figure 4.2(a), time step invariance of the statistics is well accomplished in the reference grid if Δt is less than 0.1. Grid size invariance of the statistics is also evident. As shown in figure 4.2(b), the difference of the value of statistics between reference grid and tested finest grid is less than 6%.

Figure 4.3 presents qualitative differences between the PANS calculations of various physical resolutions. Instantaneous contours of various quantities for different f_k on the plane that is perpendicular to z-axis at the near-wake of the cylinder are revealed. Figure 4.3(a)-(c) are the contours of velocity magnitude. In case of standard $K-\varepsilon$ model ($f_k = 1.0$) calculation, it can be seen that the complex near wake fluctuating motions are smeared out resulting in an unrealistically big separation bubble (fig 4.3(a)). However, as f_k value decreases, the bubble size reduces and the more details of the flow structures are captured (fig 4.3(b) and (c)). In z-vorticity contour (fig 4.3(d)-(f)), a similar pattern

of increased resolution with decreasing f_k can be seen. Contrary to the well-defined laminar type vorticity contour of $K-\varepsilon$ model (fig 4.3(d)), more complex vortical structures are captured as f_k decreases (fig 4.3(e) and (f)). Furthermore, unresolved turbulent kinetic energy levels (fig 4.3 (g)-(i)) get smaller with decreasing f_k . This clearly reveals that the implied cut-off length scale decreases with f_k . The PANS model effect can be most clearly seen on the contour plot of eddy viscosity (see equation (4.14)). Recall that the desired PANS condition for increased physical resolution is a systematic decrease in eddy viscosity. Since the unresolved dissipation rate is of the same order in high Reynolds number flow for different values of f_k , decreasing unresolved kinetic energy with f_k directly leads to decrease in eddy viscosity (fig 4.3 (j)-(l)). Considering the grid and the boundary conditions are the same for the all simulations, the increased resolution is clearly PANS model effect.

Table 4.2 shows overall statistical results for different set of calculations with various experimental results. No blockage correction is applied. The Strouhal number ($St = fD/U_0$, f : shedding frequency) is extracted from the instantaneous lift coefficient (C_L) time series. The Strouhal number is apparently insensitive to physical resolution. However, consistent with other published results⁴⁶⁻⁴⁸, the standard $K-\varepsilon$ model (case1) significantly under-predicts mean drag coefficient ($(C_D)_{\text{mean}}$) value. Since the periodic shedding motion is the main source of the momentum change in the flow over bluff body, non-physically big separation bubble in a standard $K-\varepsilon$ model simulation prevents mixing and leads to larger base pressure causing $(C_D)_{\text{mean}}$ value to be under-predicted significantly. In addition, $(C_D)_{\text{rms}}$ and $(C_L)_{\text{rms}}$ are also under-predicted in $K-\varepsilon$ model. However, as f_k decreases, more flow motions are resolved and $(C_D)_{\text{mean}}$, $(C_D)_{\text{rms}}$ and $(C_L)_{\text{rms}}$ values get closer to the experiment and LES values. The range LES values in the table come from different sub-grid models.

The profiles of the mean stream-wise velocity along the centerline are shown figure 4.4. The experimental result of Lyn⁴⁵ and Durao⁴⁴ and LES of Sohankar³³ are presented together. Following the basic philosophy of the RANS method, the RANS calculation ($f_k = 1$) of the flow past square cylinder has to result in a steady solution after a long time. However, due to RANS model inadequacy, time accurate RANS calculation yields laminar-like shedding motion with unrealistically big separation bubble. A steady RANS solution can be obtained if the calculation is performed over half domain with symmetric boundary condition along the centerline. The steady and time-accurate results are presented together in figure 4.4. If the RANS model were adequate, these two results would be identical. With PANS ($f_k = 0.7$ and 0.4), the bubble size get smaller and closer to the experimental result as f_k decreases. The stagnation point along the centerline measures $x/D = 1.3$ and 1.42 for $f_k = 0.4$ and 0.7 respectively. These values are in good agreement with Lyn's experiment ($x/D = 1.4$). On the contrary, LES result of Sohankar shows rather a small value ($x/D = 1.0$). The recovery of the stream-wise mean velocity at $x = 6.0$ is 0.74 and 0.87 for $f_k = 0.4$ and 0.7 respectively. These values are again comparable to the experiment result (Durao:0.88, Lyn:0.6) and LES result (0.79). The RMS (root-mean-square) profiles of the three fluctuating resolved velocity components are shown in figure 4.5. Again, the PANS results get closer to experimental data with decreasing f_k (fig 4.5(a), (b)). Figure 4.5(c) – the profile of $((w'w')_{\text{mean}})^{1/2}$ for PANS $f_k = 0.4$ and LES – reveals one of the apparently different features of PANS to RANS method in that the prediction of $((w'w')_{\text{mean}})^{1/2}$ profile is not even possible for the standard $K-\varepsilon$ model ($f_k = 1$) in this problem. Because there is no production for z-directional fluctuation, w' is not captured in RANS and, furthermore, there is no mean motion in spanwise direction. On the contrary, the PANS prediction of $((w'w')_{\text{mean}})^{1/2}$ for $f_k = 0.4$ comparably well follows LES result. For the case of $f_k = 0.7$, there exists

spanwise motion, but it is very small compared to the case $f_k = 0.4$. In Figure 4.6, instantaneous iso-surfaces of various flow variables (vorticity magnitude, velocity magnitude, w-velocity, x-vorticity, and y-vorticity) are compared for RANS ($f_k=1$) and PANS ($f_k=0.4$) calculations. The difference between RANS and PANS is more clearly revealed in this figure.

The lateral y-direction profiles of mean and fluctuating quantities at $x = 1.0, 2.5, 4.0,$ and 6.0 are presented in figure 4.7 and 4.8. The results are compared with Lyn's experiment. The LES data of Sohankar is presented for $x = 2.5$. For RANS ($f_k=1.0$), both mean and fluctuating profiles of the resolved velocity are far from the experimental result. However, for the PANS, getting better result decreasing f_k is observed again. Both mean and fluctuating quantities match well with experiment for $f_k = 0.7$ and 0.4 cases.

4.5 CONCLUSION

The PANS method is a recently-developed approach that attempts to combine the best features of RANS and LES. In this chapter, PANS method calculation result of flow past a square cylinder is represented. Various values of resolution control parameter ($f_k = 1.0, 0.7,$ and 0.4 with $f_\varepsilon=1.0$) are used and the results are compared with experiment and LES results. With decreasing f_k , more flow structures and scales are captured. The results show that mean drag coefficient and RMS values of drag and lift coefficients get closer to the experimental results with increasing model physical resolution (decreasing f_k). The mean and fluctuating quantities of the resolved velocity field are also compared along the centerline and at several cross-sections in near wake region. Again PANS results improve with decreasing f_k . The results typically go from RANS to experiment with decreasing f_k . Our findings indicate that PANS method is suited for performing variable resolution simulations in unsteady turbulent flows. With the proper

specification of resolution control parameter, unsteady turbulent flow calculation can be performed with less computational effort (compared to LES), with more increased accuracy (compared to standard RANS type model) using the PANS method.

Table 4.1 The computational geometry and resolution control parameter setting.

Case	Dimension	f_k	f_ε	Grid	Comment
1	$20D \times 14D \times 4D$	1.0	1.0	$95 \times 107 \times 21$	Standard RANS
2	$20D \times 14D \times 4D$	0.7	1.0	$95 \times 107 \times 21$	
3	$20D \times 14D \times 4D$	0.4	1.0	$95 \times 107 \times 21$	

Table 4.2 Summary of the PANS calculation result of integrated flow parameters in comparison with experiment and LES data.

Case	$Re/10^3$	S_t	$(C_D)_{mean}$	$(C_D)_{rms}$	$(C_L)_{rms}$
1 ($f_k=1.0$)	22	0.132	1.44	0.0022	0.27
2 ($f_k=0.7$)	22	0.133	1.77	0.129	0.994
3 ($f_k=0.4$)	22	0.130	1.97	0.216	1.19
LES ³³	22	0.126-0.132	2.03-2.32	0.16-0.20	1.23-1.54
Lyn ⁴⁵	21.4	0.132	2.1	-	-
Durao ⁴⁴	14	0.138	-	-	-
McLean ⁴⁰	15-40	-	-	-	1.4
Berman ⁴¹	5.8-32	0.130	-	-	1.2
Norberg ⁴²	13	0.132	2.16	-	-
Luo ⁴³	34	0.13	2.2	0.18	1.2

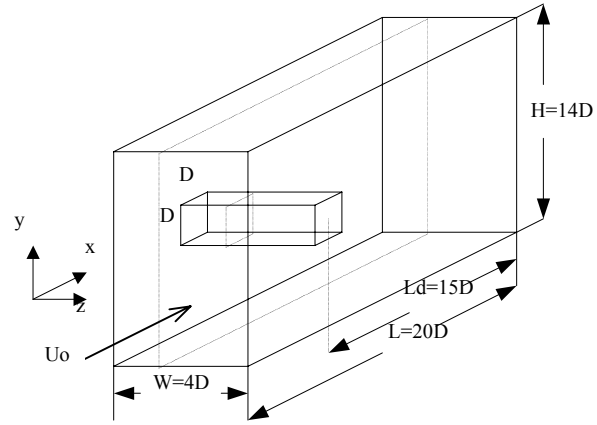
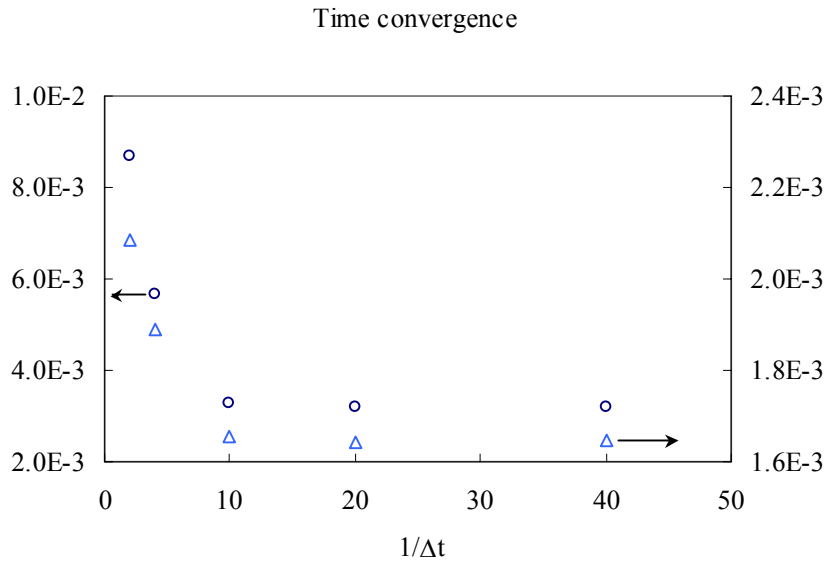
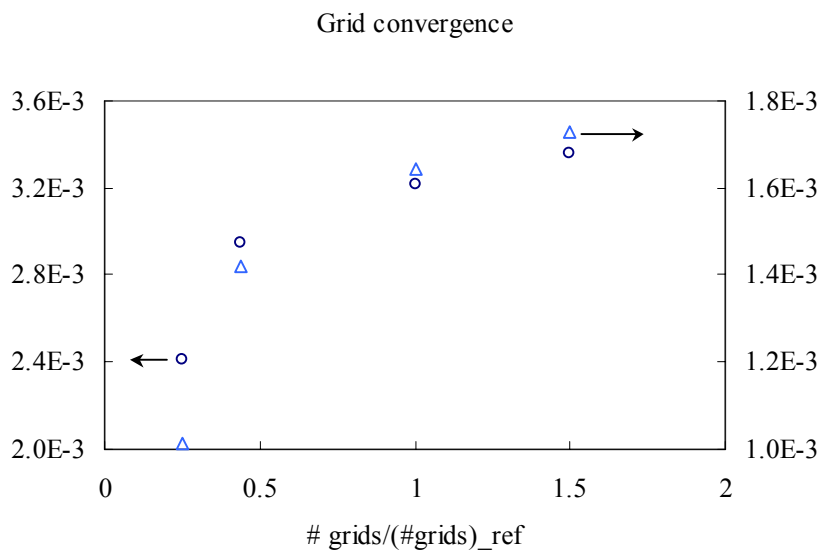


Figure 4.1 Computational domain.



(a)



(b)

Figure 4.2 Time step/grid size convergence test result of flow past a cylinder in 2D domain, (a) time step convergence test result, (b) grid size convergence test result. Symbols ○ and △ represent 2-d computational domain averaged unresolved kinetic energy and unresolved dissipation rate respectively.

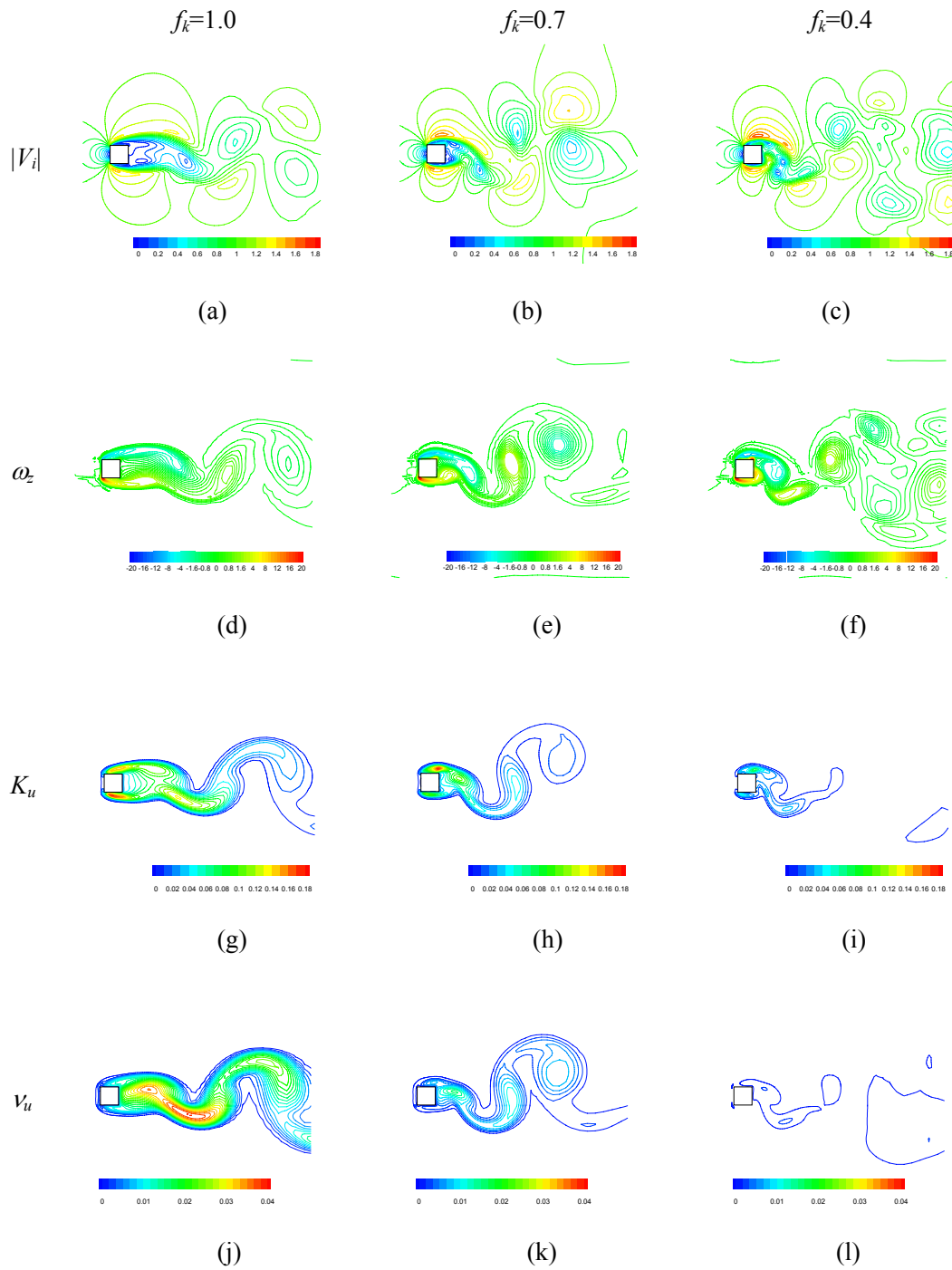


Figure 4.3 Instantaneous contour plot of velocity magnitude (a-c), z-vorticity (d-f), unresolved kinetic energy (g-i), and unresolved eddy viscosity (j-l) for various f_k value.

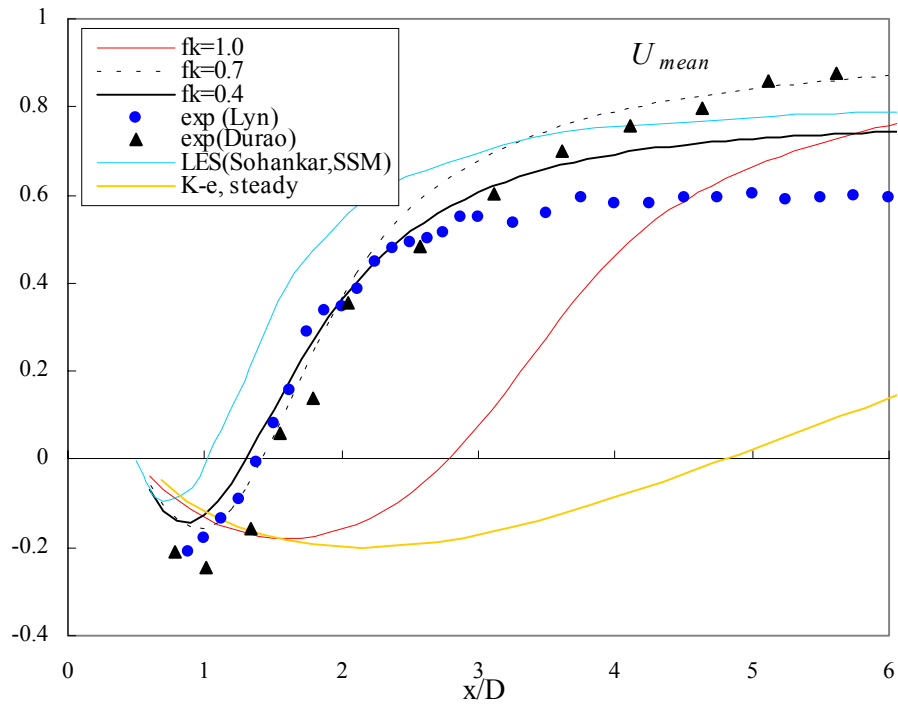


Figure 4.4 Stream-wise mean velocity profiles along the centerline.

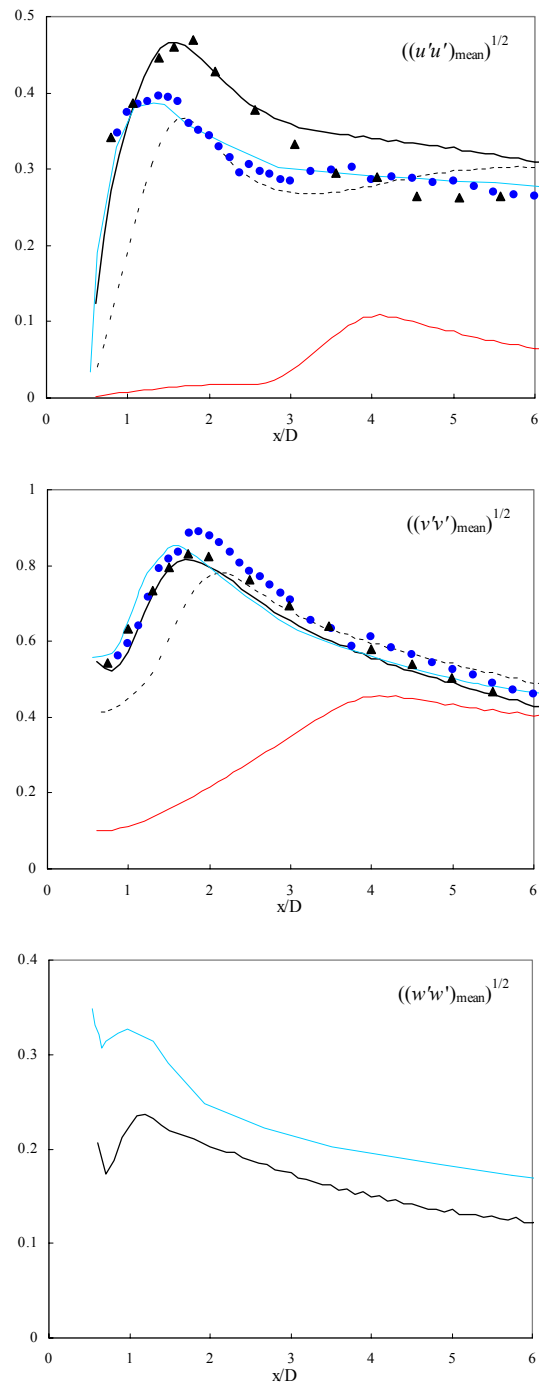


Figure 4.5 Profiles of $((u'u')_{\text{mean}})^{1/2}$, $((v'v')_{\text{mean}})^{1/2}$, and $((w'w')_{\text{mean}})^{1/2}$ along the centerline. Legend is the same as given in Fig 4.4.

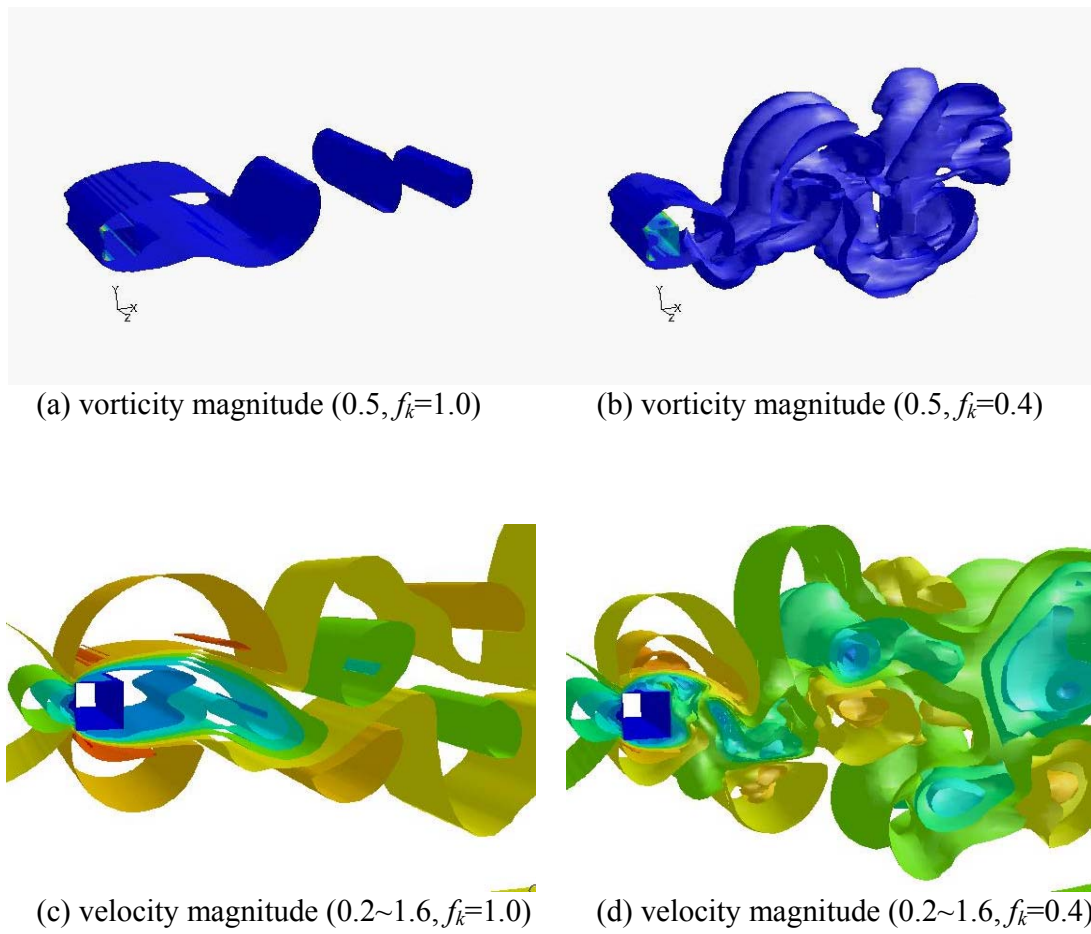


Figure 4.6 Instantaneous iso-surfaces, (a)-(b) vorticity magnitude, (c)-(d) velocity magnitude, (e)-(f) z-velocity, (g)-(h) x-vorticity, and (i)-(j) y-vorticity. Values in the parenthesis represent the magnitude of each iso-surface.

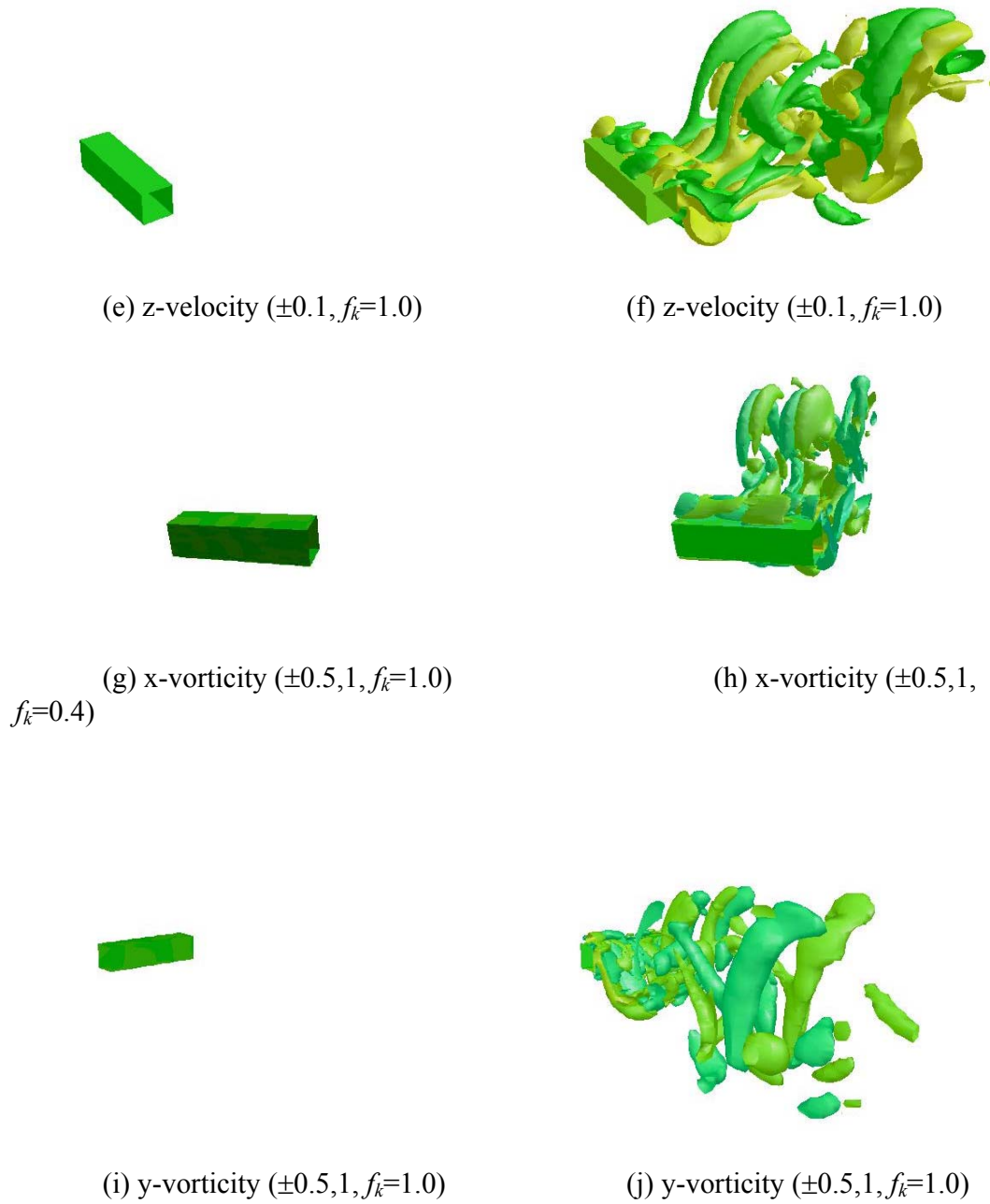


Figure 4.6 (Continued)

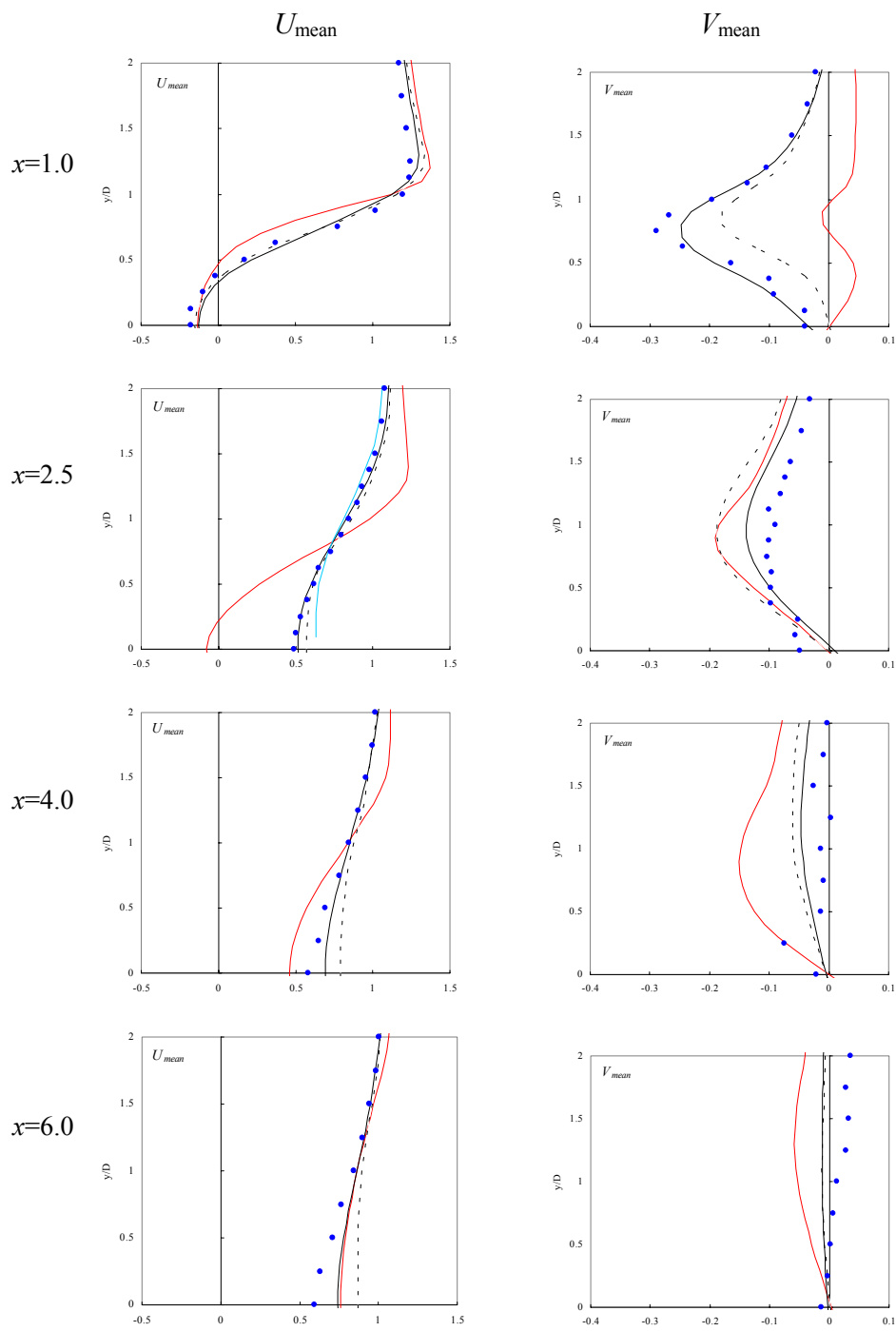


Figure 4.7 Lateral profiles of mean velocities at various x -locations. Legend is the same as given in Fig 4.4.

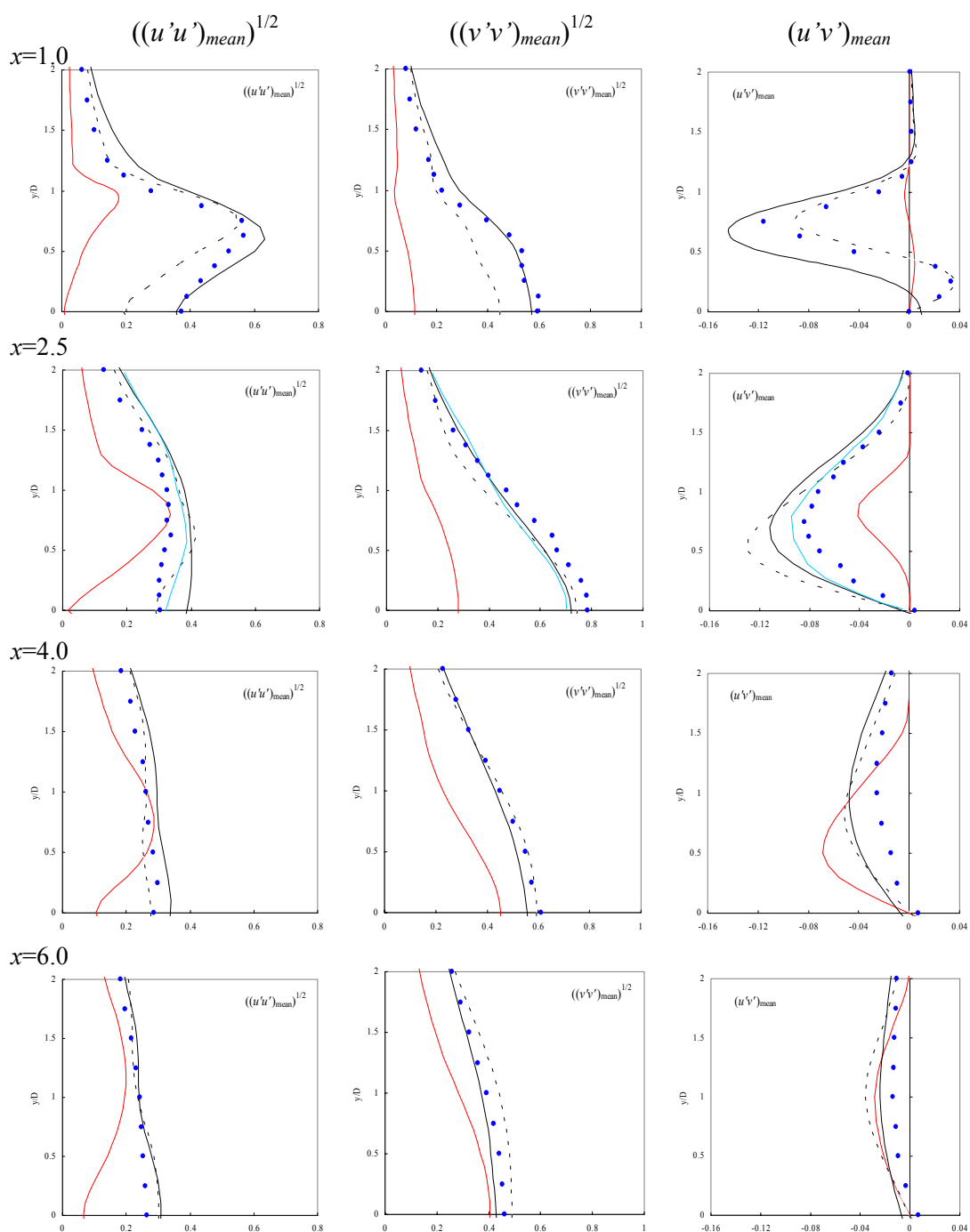


Figure 4.8 Lateral profiles of turbulent quantities at various x -locations. Legend is the same as given in Fig 4.4.

REFERENCES

1. Wm. T. Ashurst, A. R. Kerstein, R. M. Kerr, and C. H. Gibson, "Alignment of vorticity and scalar gradient with strain rate in simulated Navier–Stokes turbulence," *Phys. Fluids* **30**, 2343 (1987).
2. S. S. Girimaji and S. B. Pope, "A diffusion model for velocity gradients in turbulence," *Phys. Fluids A* **2**, 242 (1990).
3. B. J. Cantwell, "Exact solution of a restricted Euler equation for the velocity gradient tensor," *Phys. Fluids A* **4**, 782 (1992).
4. B. J. Cantwell, "On the behavior of velocity gradient tensor invariants in direct numerical simulations of turbulence," *Phys. Fluids A* **5**, 2008 (1993).
5. S. S. Girimaji and C. G. Speziale, "A modified restricted Euler equation for turbulent flows with mean velocity gradients," *Phys. Fluids* **7**, 1438 (1995).
6. J. Soria, R. Sondergaard, B. J. Cantwell, M. S. Chong, and A. E. Perry, "A study of the fine-scale motions of incompressible time-developing mixing layers," *Phys. Fluids* **6**, 871 (1994).
7. J. Martin, A. Ooi, C. Dopazo, M. S. Chong, and J. Soria, "The inverse diffusion time scale of velocity gradients in homogeneous isotropic turbulence," *Phys. Fluids* **9**, 814 (1997).
8. J. Martin, C. Dopazo, and L. Valino, "Dynamics of velocity gradient invariants in turbulence: Restricted Euler and linear diffusion models," *Phys. Fluids* **10**, 2012 (1998).
9. J. Martin, A. Ooi, M. S. Chong, and J. Soria, "Dynamics of the velocity gradient tensor invariants in isotropic turbulence," *Phys. Fluids* **10**, 2336 (1998).
10. A. Ooi, J. Martin, J. Soria, and M. S. Chong, "A study of the evolution and characteristics of the invariants of the velocity-gradient tensor in isotropic turbulence," *J. Fluid Mech.* **381**, 141 (1999).

11. P. Vieillefosse, "Local interaction between vorticity and shear in a perfect incompressible fluid," *J. Phys. (Paris)* **43**, 837 (1982).
12. M. S. Chong, A. E. Perry, and B. J. Cantwell, "A general classification of three-dimensional flow fields," *Phys. Fluids A* **2**, 765 (1990).
13. Sharath S. Girimaji, "Modeling turbulent scalar mixing as enhanced diffusion," *Combust. Sci. and Tech.* **97**, 85 (1994).
14. P.K. Yeung, private communication, (1999).
15. S. Crow, "Viscoelastic properties of fine-grained turbulence," *J. Fluid Mech.* **33**, 1 (1968).
16. W. C. Reynolds and S. C. Kassinos, "A one-point model for the evolution of the Reynolds stress and structure tensors in rapidly deformed homogeneous turbulence," *Proc. R. Soc. London, Ser. A*, **451**, 87 (1995).
17. S. C. Kassinos, W. C. Reynolds, and M. M. Rogers, "One-point turbulence structure tensors," *J. Fluid Mech.* **428**, 213 (2001).
18. J. L. Lumley, "Computational modeling of turbulent flows," *Adv. Appl. Mech.* **18**, 123 (1978).
19. S. S. Girimaji, "Pressure-strain correlation modeling of complex turbulent flows", *J. Fluid Mech.* **422**, 91 (2000).
20. J. C. Rotta, "Statistische theorie nichthomogener turbulenz 1," *Z.Phys.* **129**, 547 (1951).
21. J. C. R. Hunt and D. J. Carruthers, "Rapid distortion theory and the problems of turbulence," *J. Fluid Mech.* **212**, 497 (1990).
22. K. R. Sreenivasan and R. Narasimha, "Rapid distortion of axisymmetric turbulence," *J. Fluid Mech.*, **84**, 497 (1978).
23. M. R. Maxey, "Distortion of turbulence in flows with parallel streamlines," *J. Fluid.Mech.*, **124**, 261 (1982).
24. B. E. Launder. G. J. Reece, and W. Rodi, "Progress in the development of a Reynolds stress turbulent model," *J. Fluid.Mech.*, **68**, 537 (1973).
25. S. B. Pope, *Turbulent Flows*, Cambridge University Press, Cambridge (2000).

26. C. Cambon and J. F. Scott, "Linear and nonlinear models of anisotropic turbulence," *Annual Rev. Fluid Mech.* **31**, 1 (1999).
27. S. C. Kassinos and W. C. Reynolds, "A particle representation model for the deformation of homogeneous turbulence," *Annual Research Briefs, Center for Turbulence Research, NASA Ames/Stanford University, Stanford, CA*, p31 (1996).
28. D. Naot, A. Shavit, and M. Wolfshtein, "Interactions between components of the turbulent velocity correlation tensor due to pressure fluctuations," *Israel J. Technol.* **8**, 259 (1970).
29. C. G. Speziale, S. Sarkar, and T. B. Gatski, "Modeling the pressure-strain correlation of turbulence: An invariant dynamical systems approach," *J. Fluid Mech.*, **227**, 245 (1991).
30. A. Sambasivam, "Realizability of Reynolds stress and rapid pressure-strain correlation models in turbulence," MS Thesis, Aerospace Engineering Department, Texas A&M University (2003).
31. W. Rodi, J. Ferziger, M. Breuer, and M. Pourquie, 1997, "Status of large eddy simulation : Result of workshop," *ASME J. Fluids Eng.*, **119**, 248 (1997).
32. P. R. Voke, "Flow past a square cylinder : Test case LES2," in J. P. Chollet, P. R. Voke, and L. Kouser (eds.), *Direct and Large Eddy Simulation II*, Kluwer Academic, Dordrecht (1997).
33. A. Sohankar and L. Davidson, "Large eddy simulation of flow past a square cylinder : Comparison of different subgrid scale models," *ASME J. Fluids Eng.*, **122**, 39 (2000).
34. P. R. Spalart, "Trends in turbulence treatments," AIAA paper 2000-2306, *Fluids 2000 Conference and Exhibit, Denver, CO*, (2000).
35. P. Batten, U. Goldberg, and S. Chakravarthy, "LNS-An Approach towards embedded LES," AIAA paper No.2002-0427, 40th Aerospace Sciences Meeting and Exhibit, Reno, NV, (2002).
36. M. R. Khorrami, B. Singer, and M. E. Berkman, "Time accurate simulations and acoustic analysis of slat free shear layer," *AIAA Journal*, **40**, 7, 1284 (2002).

37. C. G. Speziale, "Computing non-equilibrium flows with time-dependant RANS and VLES," Proceedings of the 15th ICNMF, Monterey, CA, USA (1996).
38. S. S. Girimaji, "Partially averaged Navier-Stokes method : A variable resolution (from RANS to DNS) turbulence model," Submitted to Physics of Fluids (2003).
39. M. Germano, "Turbulence : The filtering approach," J. Fluid Mech., **238**, 325 (1992).
40. I. McLean, and I. Gartshore, "Spanwise correlations of pressure on a rigid square section cylinder," J. Wind Eng. Ind. Aerodyn., **41-44**, 797 (1992).
41. P. W. Berman, and E. D. Obasaju, "An experimental study of pressure fluctuations on fixed and oscillating square-section cylinders," J. Fluid Mech., **119**, 297 (1982).
42. C. Norberg, "Flow around rectangular cylinders : Pressure forces and wake frequencies," J. Wind Eng. Ind. Aerodyn., **49**, 187 (1993).
43. S. C. Luo, M. G. Yazdani, Y. T. Chew, and T. S. Lee, "Effects of incidence and afterbody shape on flow past bluff cylinders," J. Wind Eng. Ind. Aerodyn., **53**, 375 (1994).
44. D. F. G. Durao, M. V. Heitor, and J. C. F. Pereira, "Measurements of turbulent and periodic flows around a square cross-section cylinder," Exp. Fluids, **6**, 298 (1988).
45. D. A. Lyn, S. Einav, W. Rodi, and J. H. Park, "A laser-doppler velocimetry study of the ensemble-averaged characteristics of the turbulent near wake of a square cylinder," J. Fluid Mech., **304**, 285 (1995).
46. R. Franke and W. Rodi, "Calculation of vortex shedding past a square cylinder with various turbulence models," in Schumann, U. et. al. (eds.), *Turbulent Shear Flows 8*, Springer, Berlin (1993).
47. S. Murakami and A. Mochida, "On turbulent vortex shedding flow past 2D square cylinder predicted by CFD," J. Wind Eng. Ind. Aerodyn., **54/55**, 191 (1995).
48. W. Rodi, "Comparison of LES and RANS calculation of the flow around bluff bodies," J. Wind Eng. Ind. Aerodyn., **69-71**, 55 (1997).

APPENDIX A

The RDT results show (Table 2) that in the following cases: 1C1, 1C3 (for all mean flows), 1C2 (AC, AE, PS), 2C1(AC, AE), and 2C2(HS), initial anisotropy of turbulence does not change. These are cases, when the production-of-anisotropy term P''_{ij} in equation (16) is equal to zero for all Reynolds stresses at $t = 0$.

As an example, let us consider the mean flow under axisymmetric contraction, where $U_{1,1} = S$, $U_{2,2} = U_{3,3} = -S/2$, and the rest of the components is equal to zero. In such a flow, the components of the Reynolds stress production tensor

$$P_{ij} = -\langle u_i u_k \rangle \frac{\partial U_j}{\partial x_k} - \langle u_j u_k \rangle \frac{\partial U_i}{\partial x_k}$$

are $P_{11} = -2S \langle u_1 u_1 \rangle$, $P_{22} = S \langle u_2 u_2 \rangle$, $P_{33} = S \langle u_3 u_3 \rangle$, and the others are equal to zero. For different initial turbulence anisotropy cases one has

$$1C1: \langle u_1 u_1 \rangle = 2k, \quad P_{11} = -4Sk, \quad P_{22} = P_{33} = 0, \quad 2P = -4Sk,$$

$$1C2: \langle u_2 u_2 \rangle = 2k, \quad P_{22} = 2Sk, \quad P_{11} = P_{33} = 0, \quad 2P = 2Sk,$$

$$1C3: \langle u_3 u_3 \rangle = 2k, \quad P_{33} = 2Sk, \quad P_{11} = P_{22} = 0, \quad 2P = 2Sk,$$

$$2C1: \langle u_1 u_1 \rangle = 0, \quad \langle u_2 u_2 \rangle = \langle u_3 u_3 \rangle = k, \quad P_{11} = 0, \quad P_{22} = P_{33} = Sk, \quad 2P = 2Sk,$$

$$2C2: \langle u_2 u_2 \rangle = 0, \quad \langle u_1 u_1 \rangle = \langle u_3 u_3 \rangle = k, \quad P_{11} = -2kS, \quad P_{22} = 0, \quad P_{33} = Sk, \\ 2P = -Sk,$$

$$2C3: \langle u_3 u_3 \rangle = 0, \quad \langle u_1 u_1 \rangle = \langle u_2 u_2 \rangle = k, \quad P_{11} = -2kS, \quad P_{22} = Sk, \quad P_{33} = 0, \\ 2P = -Sk.$$

Then, the components of the production-of-anisotropy tensor $P''_{ij} = P_{ij} - 2Pb_{ij} - \frac{2}{3}\delta_{ij}P$

in each case are

$$1C1: P''_{11} = P''_{22} = P''_{33} = 0,$$

$$1C2: P''_{11} = P''_{22} = P''_{33} = 0,$$

$$1C3: P''_{11} = P''_{22} = P''_{33} = 0,$$

$$2C1: P''_{11} = P''_{22} = P''_{33} = 0,$$

$$2C2: P''_{11} = -\frac{3}{2}Sk, P''_{22} = 0, P''_{33} = \frac{3}{2}Sk,$$

$$2C3: P''_{11} = -\frac{3}{2}Sk, P''_{22} = \frac{3}{2}Sk, P''_{33} = 0.$$

Non-diagonal components of P''_{ij} are equal to zero in all cases. It is seen that only in two cases (2C2 and 2C3) there are non-zero components of P''_{ij} and, therefore, the invariant $P''_{ij}P''_{ij}$ has a non-zero value. In these two cases, the RDT data show the turbulence anisotropy evolution from the initial level. In other cases (1C1, 1C2, 1C3, and 2C1) there is no production of anisotropy and, as RDT computations demonstrate, no change of initial anisotropy occurs. It follows then from equation (16), that the pressure-strain tensor components have to be also equal to zero in such cases.

For other mean flow configurations, similar analysis can be easily made, which leads to the same conclusions.

VITA

Eun-Hwan Jeong was born in Jinju, Korea in 1968. He received his B.S. degree in February 1991 and M.S. degree in February 1993 from mechanical and aerospace engineering department of Korea Advanced Institute of Science and Technology respectively. From February 1993 to May 1999, he worked as a researcher in the area of gas turbine cycle analysis and air-cycle machine development in Samsung Aerospace Industries. He enrolled in the graduate program in aerospace engineering at Texas A&M University in Sep 1999 and earned his Doctor of Philosophy (Ph.D.) in December 2003. His area of interest is fluid dynamics and turbulence modeling.

Mr. Jeong can be reached through Dr. Sharath S. Girimaji at the Aerospace Engineering Department of Texas A&M University, College Station, TX 77843-3141.